JGR Solid Earth

RESEARCH ARTICLE
10.1029/2018JB017106

Key Points:
- Late Paleozoic bimodal rocks comprising asthenosphere-derived mafic rock and metasediment-derived granite have been discovered in southern Tibet
- The Lhasa was once a microcontinent within Paleo-Tethyan Ocean and the bimodal magmatism was caused by northward subduction of oceanic slab
- The microcontinent represented by the southern Lhasa Block was transformed into juvenile terrane by Phanerozoic crustal growth and reworking

Supporting Information:
- Supporting Information S1
- Table S1
- Table S2
- Table S3
- Table S4

Correspondence to:
L. Ma and Q. Wang,
malin@gig.ac.cn;
wqiang@gig.ac.cn

Citation:
Ma, L., Kerr, A. C., Wang, Q., Jiang, Z.-Q., Tang, G.-J., Yang, J.-H., et al. (2019). Nature and evolution of crust in southern Lhasa, Tibet: Transformation from microcontinent to juvenile terrane. *Journal of Geophysical Research: Solid Earth*, *124*, 6452–6474. https://doi.org/10.1029/2018JB017106

Received 1 DEC 2018
Accepted 19 JUN 2019
Accepted article online 26 JUN 2019
Published online 13 JUL 2019

Nature and Evolution of Crust in Southern Lhasa, Tibet: Transformation From Microcontinent to Juvenile Terrane

Lin Ma[1,2], Andrew C. Kerr[2], Qiang Wang[1,3,4], Zi-Qi Jiang[1], Gong-Jian Tang[1,3], Jin-Hui Yang[5], Xiao-Ping Xia[1], Wan-Long Hu[1,4], Zong-Yong Yang[1,4], and Peng Sun[1,4]

[1]State Key Laboratory of Isotope Geochemistry, Guangzhou Institute of Geochemistry, Chinese Academy of Sciences, Guangzhou, China, [2]School of Earth and Ocean Sciences, Cardiff University, Cardiff, UK, [3]Centre for Excellence in Tibetan Plateau Earth Sciences, CAS, Beijing, China, [4]Earth and Planetary Sciences, University of Chinese Academy of Sciences, Beijing, China, [5]Institute of Geology and Geophysics, Chinese Academy of Sciences, Beijing, China

Abstract The nature and pre-Cenozoic evolution history of crust in southern Lhasa, which is crucial for our understanding of Indo-Asian continental collision and Tibetan uplift during the Cenozoic, remains controversial due to a "missing" pre-Mesozoic magmatic record. In this contribution, we report petrological and geochemical data for newly identified Paleozoic bimodal magmatism in the Zhengga area of southern Tibet. The magmatism comprises Late Devonian-Early Carboniferous (366–353 Ma) amphibolite and two-mica gneissic granite. The protoliths of the Zhengga amphibolite were gabbro and diorite with low SiO_2 and high MgO, Cr, and Ni contents with high $\varepsilon_{Nd}(t)$ values of +3.3 to +8.0, variable and positive zircon $\varepsilon_{Hf}(t)$ of +0.9 to +11.2, and low zircon $\delta^{18}O$ of 5.7 ± 0.2‰. These protoliths are proposed to have formed by decompression melting of asthenosphere during intracontinental back-arc extension. In contrast, the granite has relatively high SiO_2 and low MgO contents with much lower $\varepsilon_{Nd}(t)$ of −8.6 to −7.3, variable and negative zircon $\varepsilon_{Hf}(t)$ of −10.4 to −1.3, and high zircon $\delta^{18}O$ of 9.4 ± 0.2‰ values and was most likely derived from an ancient metasedimentary source. This magma subsequently underwent recharge with minor amounts mafic magma followed by fractional crystallization of K-feldspar in middle-upper crust (~10–20 km) magma chambers. Using our new data, in combination with Nd-Hf isotopes, we present the first comprehensive picture of crustal evolution in southern Lhasa. The southern Lhasa sub-block is likely to have been a microcontinent that underwent extensive Phanerozoic crustal reworking and growth, rather than a Mesozoic-Early Tertiary juvenile accretionary arc terrane.

1. Introduction

The continental crust is the primary archive of Earth history and provides a synoptic view deep into Earth history (e.g., Jagoutz et al., 2009; Kemp & Hawkesworth, 2014; Korenaga, 2018; Spencer et al., 2017, and references therein). However, information on the origin and evolution of continental crust, in addition to the rate of growth, is fragmented, as large volumes of continental crust have been reworked and recycled back into the mantle by a variety of processes.

At present, ~70% of the continental crust is younger than 1 Ga, and only ~5% is of Archean age (2.5–4 Ga; cf. Korenaga, 2018). This is principally due to crustal reworking in young orogens, where information on nature and evolutionary history of continental crust are lost or hidden as a result of orogenic overprinting and recycled to the mantle via erosion and subduction (e.g., Amelin et al., 1999; Hawkesworth & Kemp, 2006). Interpreting the information from early geological record is crucial for understanding evolution of continental crust through time and establishing the geodynamic controls on the formation of continent (Belousova et al., 2010; Collins et al., 2011; Dhuime et al., 2012; Kemp & Hawkesworth, 2014).

The Gangdese batholith extends for over 1,500 km across the southern Lhasa Block of Tibet and consists of the Mesozoic to Cenozoic granitoids with depleted mantle-like Nd-Hf isotopic signatures, indicating significant Mesozoic or early Cenozoic crustal growth (e.g., Ji et al., 2009; Ma et al., 2013; Niu et al., 2013; Wei et al., 2017; Zhu et al., 2011, 2013). Southern Lhasa thus is therefore considered to represent juvenile crust that was accreted to central Lhasa in the Permian-Early Tertiary (e.g., Ji et al., 2009). Recently, numerous inherited zircons of Proterozoic and Paleozoic age have been identified in the Gangdese granitic batholith and these zircons indicate potential Precambrian basement beneath southern Lhasa (e.g., Dong et al., 2010; Guo

et al., 2016; Lin et al., 2013; Xu et al., 2013). However, few pre-Permian magmatic rocks have been found in southern Lhasa and this limits our understanding of the compositional evolution of continent and dynamic history in southern Lhasa (e.g., Dong et al., 2014; Guo et al., 2016; Ji et al., 2012; Metcalfe, 2006, 2013; Zhu et al., 2013).

In this contribution, we report zircon U-Pb chronology and geochemical data from newly identified Late Paleozoic bimodal magmatism in southern Lhasa. These data, together with stratigraphic and petrographic evidence, provide a robust geological record and are used to (1) assess the petrogenesis and geodynamic setting of the Late Devonian magmatism in southern Lhasa, (2) reconstruct paleogeographic position of the southern Lhasa in the latest Devonian, and (3) reveal crustal evolution history in the southern Lhasa.

2. Geological Background and Sample Description

From south to north, Himalayan-Tibetan Orogen consists of the Himalaya, Lhasa, Western Qiangtang, Eastern Qiangtang, and Songpan-Ganze blocks (Yin & Harrison, 2000; Zhu et al., 2013). These blocks are separated by a series of suture zones, namely, the Indus-Yarlung Tsangpo, Bangong-Nujiang, Longmu Tso-Shuanghu, and Jinsha Suture Zones (Figure 1).

The Lhasa Block represents the southernmost part of the pre-Cenozoic Asian continent and is bounded by the Indus-Yarlung Tsangpo suture to the south and the Bangong-Nujiang suture to the north (Figure 1; Yin & Harrison, 2000). It is generally accepted that the Bangong-Nujiang suture formed during the Late Jurassic-middle Cretaceous and the Indus-Yarlung Tsangpo suture marks the closure of the Tethyan ocean during the Paleocene-Eocene (e.g., Aitchison et al., 2003; Chung et al., 2005; Wu et al., 2014; Yin & Harrison, 2000; Zhu et al., 2013). Based on the distribution of different sedimentary cover rocks and ophiolites, the Lhasa Block has been divided into northern, central, and southern subblocks, separated by the Shiquan River-Nam Tso Mélange Zone and Luobadui-Milashan Fault, respectively (Figure 1; Zhu et al., 2011, 2013).

The northern subblock mostly comprises Triassic-Cenozoic sedimentary and Cretaceous magmatic rocks (Leier et al., 2007; Zhu et al., 2013, and references therein; Figure S1 in the supporting information), indicating the existence of juvenile crust rather than reworked ancient crust beneath this subblock (Zhu et al., 2011, 2013). In addition, Precambrian basement rocks (Amdo orthogneiss) that represent an augen-shaped microcontinent (~150 km long by 80 km wide at its maximum extent) are found in the Amdo area, between northern Lhasa and western Qiangtang (Guynn et al., 2006; Zhu et al., 2013).

The central subblock retains the most complete sedimentary record in the region and comprises a Carboniferous-Permian metasedimentary sequence and a Late Jurassic-Early Cretaceous volcanosedimentary sequence, with minor Ordovician, Silurian, and Triassic limestone (Kapp et al., 2007; Leier et al., 2007; Zhu et al., 2010, 2013) along with rare Precambrian strata (Dong et al., 2011; Figure S1), indicating the presence of a Precambrian basement in the central subblock (Zhu et al., 2013). The Late Carboniferous to Permian (ca. 301–262 Ma) Sumdo eclogite is exposed along the southern margin of the central Lhasa subblock (Figures 1 and 2) and represents a remnant of Paleo-Tethyan oceanic lithosphere (Li et al., 2009; Yang et al., 2009).

The southern Lhasa subblock (the Gangdese area) is characterized by extensive Mesozoic-Cenozoic intrusive and volcanic rocks (e.g., Chu et al., 2006; Ji et al., 2009; Lee et al., 2009; Wen et al., 2008; Zhu et al., 2013), and coeval granulite and amphibolite facies metamorphic rocks (e.g., Dong et al., 2011; Zhang et al., 2010). Thus, the southern subblock has also been considered to represent juvenile crust without Precambrian basement, similar to the northern Lhasa sub-block (Ji et al., 2009; Zhu et al., 2011). However, recent studies on some of the granitoids in the southern subblock have yielded Early Paleozoic and Paleo- and Meso-Proterozoic ages (Figures 1 and 2; Dong et al., 2010; Lin et al., 2013).

Late Devonian-Early Carboniferous intrusive rocks have been found in the Gyaca and Nang areas of the eastern Gangdese segment (Figure 2) and are interpreted as a bimodal igneous association formed in back-arc extensional setting (Dong et al., 2014; Ji et al., 2012; Wu et al., 2014; Zhu et al., 2013). The Zhengga Devonian magmatic rocks, which are the focus of this paper, are composed of two-mica gneissic granites and amphibolite suites that are located to the north of the Luobusa ophiolite in the eastern Gangdese (Figure 2). The rocks are foliated and metamorphosed to greenschist and amphibolite-facies

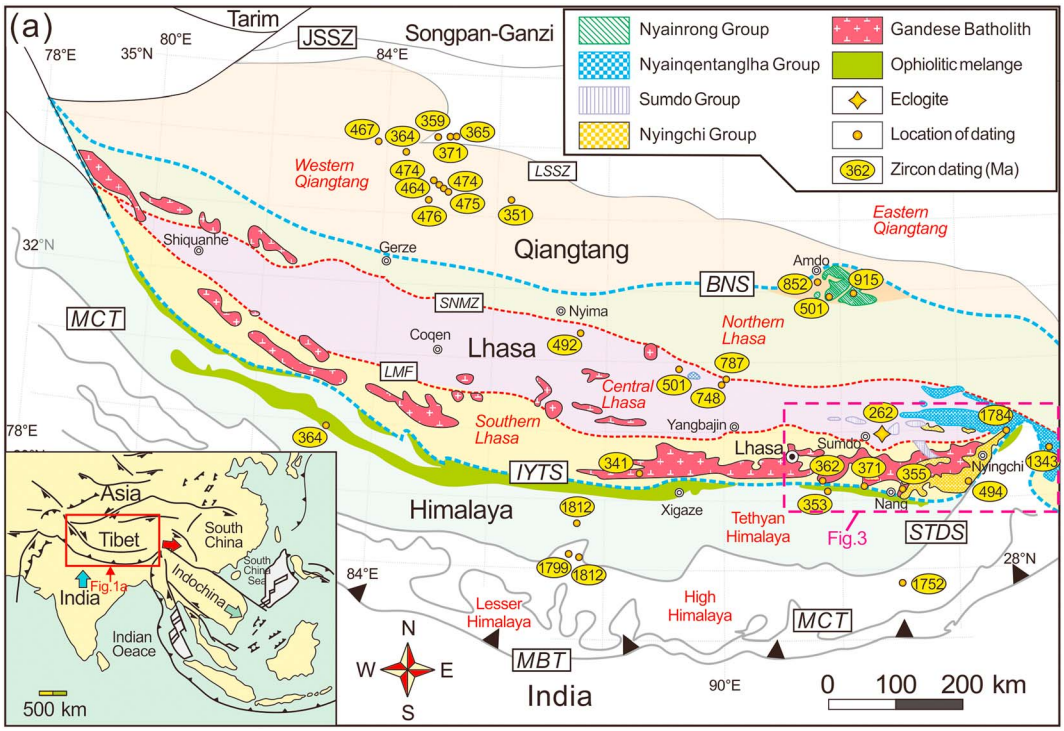

Figure 1. Distribution and zircon ages of the Proterozoic-Carboniferous rocks and Sumdo eclogite in the central-southern Tibetan Plateau (modified from Zhu et al., 2013). Abbreviations: JSSZ = Jinsha Suture Zone; LSSZ = Longmu Tso-Shuanghu Suture Zone; BNSZ = Bangong-Nujiang Suture Zone; SNMZ = Shiquan River-Nam Tso Mélange Zone; LMF = Luobadui-Milashan Fault; IYTS = Indus-Yarlung Tsangpo Suture Zone.

(Figures 3a and 3b). These Zhengga magmatic rocks mostly show a gneissic structure and were intruded by Cretaceous gabbros (Ma et al., 2013) and Paleocene granitoids (Ma et al., 2017). Some amphibolites occur as (2–20 cm diameter) enclaves within the two-mica granites (Figure 3c).

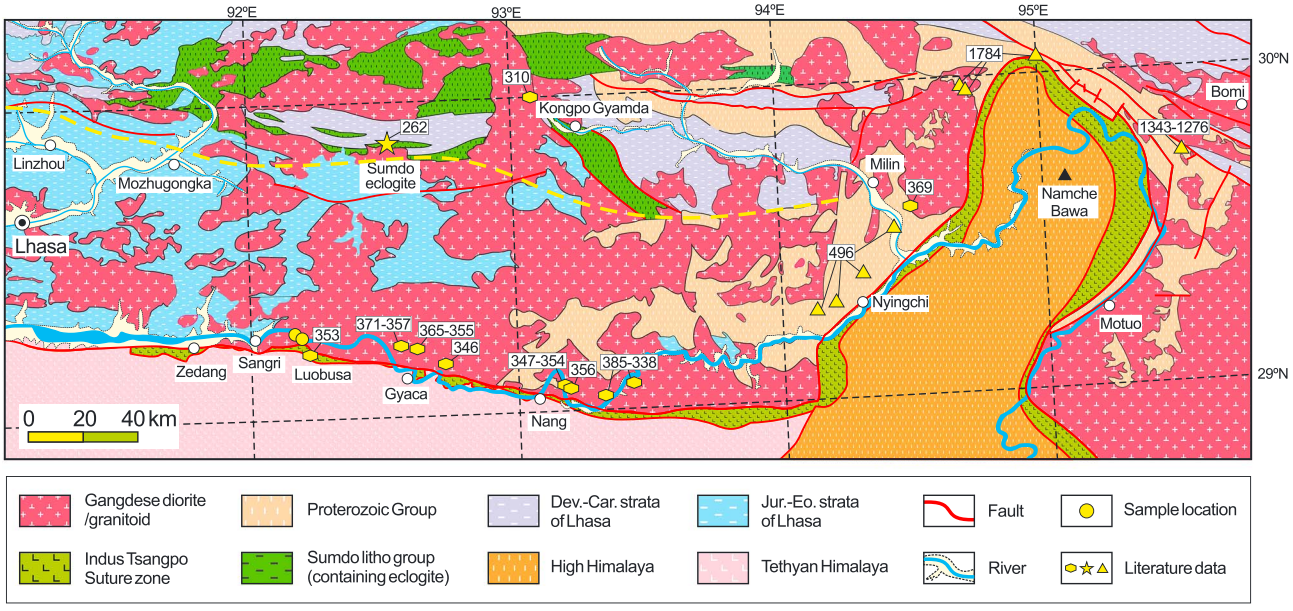

Figure 2. Outcrops of granitoids in the eastern Lhasa Block. The yellow dashed line shows boundary between the southern and central Lhasa subblocks. Literature data include granitoid/rhyolite (hexagon), Sumdo eclogite (star), and Precambrian rocks (triangle). Data sources include Lee et al. (2009), (2010, 2014), Ji et al. (2012), Lin et al. (2013), and Xu et al. (2013).

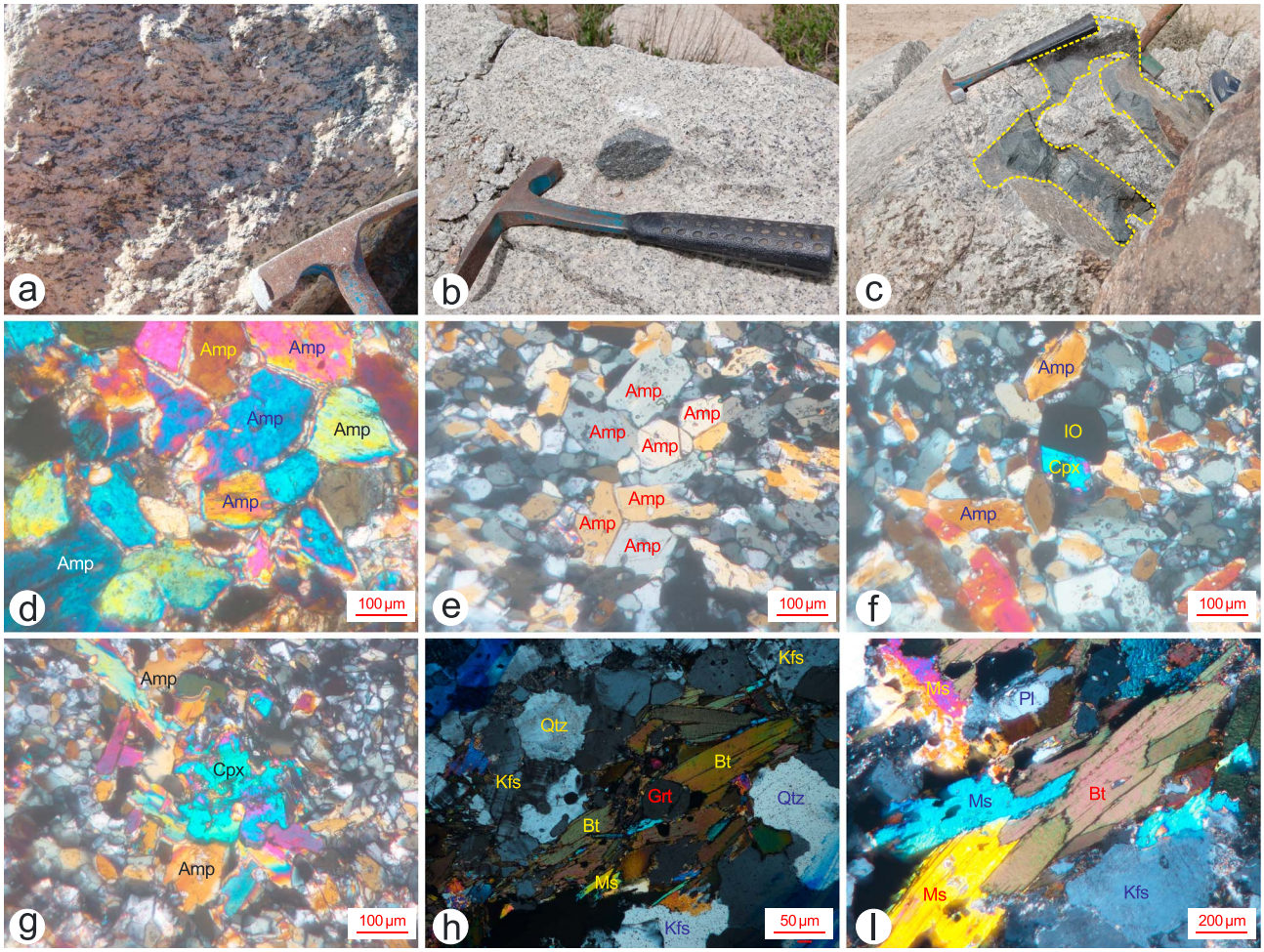

Figure 3. Field geological characteristics and petrography of the Zhengga amphibolite and two-mica granite: (a) field outcrop of two-mica granite; (b) mafic enclave; (c) interconnection of amphibolite and granite; (d–g) main mineral assemblage of the amphibolite; and (h, i) main mineral assemblage of the two-mica granite. Abbreviation: Pl, plagioclase; Grt, garnet; Bt, biotite; Cpx, clinopyroxene; Ms, muscovite; Qtz, quartz; Amp, amphibole; Kfs, potassium feldspar; IO, iron oxide.

The two-mica gneissic granite is composed of quartz (~30–40 vol.%), potassium feldspar (~30–35 vol.%), plagioclase (~5–10 vol.%), biotite (~10–15 vol.%), and muscovite (~5–8 vol.%) with minor garnet and Fe-oxides (Figures 3h and 3i). The amphibolites mainly exhibit massive and medium- to fine-grained granular and lepidoblastic textures and in addition to amphibole (~45 vol.%) contain plagioclase (~40 vol.%) with minor Fe oxides (Figures 3d–3g). These rocks are similar to the coeval biotite gneisses and amphibolites found in Gyaca and Nang areas (Dong et al., 2014; Ji et al., 2012). Clinopyroxene crystals in the Zhengga amphibolites are rare and are typically embedded in amphiboles as relict crystals (Figures 3f and 3g).

3. Analytical Methods

Cathodoluminescence (CL) imaging of zircon was performed at the State Key Laboratory of Isotope Geochemistry (SKLaBIG) Guangzhou Institute of Geochemistry Chinese Academy of Sciences (GIG CAS). U-Pb isotope compositions of zircon grains from two amphibolite and three two-mica granite samples were analyzed using a Cameca IMS-1280HR secondary ion mass spectrometer (SIMS) at the SKLaBIG GIG CAS and the Cameca IMS-1280 SIMS at the Institute of Geology and Geophysics (IGG) CAS in Beijing, respectively. Zircon U-Th-Pb isotopic ratios were corrected using the standard zircon Plešovice (Sláma et al., 2008) and Qinghu (Li et al., 2013) based on an observed linear relationship between $\ln(^{206}Pb/^{238}U)$ and $\ln(^{238}U^{16}O_2/^{238}U$; Whitehouse et al., 1997). The weighted mean U-Pb ages and Concordia plots were

processed using the Isoplot v.3.0 program (Ludwig, 2003). In this study, 17 Qinghu zircon spots yield a mean age of 159.4 ± 1.2 Ma (2σ, Mean Square Weighted Deviation [MSWD] = 0.72), which is identical to the recommended value of 159.5 ± 0.2 Ma within error (Li et al., 2013). The standard zircon Plešovice yielded a weighted $^{206}Pb/^{238}U$ age of 336.9 ± 2.1 Ma (2σ, MSWD = 0.3, n = 23), which is in good agreement with the recommended U-Pb ages ($^{206}Pb/^{238}U$ = 337.13 ± 0.37 Ma) within errors (Sláma et al., 2008).

Laser ablation inductively coupled plasma mass spectrometer (LA-ICP-MS) zircon U-Pb dating of one amphibolite sample 16ML05-2 was carried out by multicollector (MC)-ICP-MS at the IGG CAS in Beijing. An Agilent 7500a quadruple (Q)-ICPMS and a Neptune multicollector (MC)-ICPMS with a 193-nm excimer ArF laser-ablation system (GeoLas Plus) attached were used for simultaneous determination of zircon U-Pb ages. During the analyses in this study, the standard zircon MUD Tank yielded a weighted $^{206}Pb/^{238}U$ age of 732.2 ± 3.5 Ma (2σ, MSWD = 0.024, n = 8), which is identical to the recommended value of 731.9 ± 3.4 Ma within error (Yuan et al., 2008).

Rock samples were first examined by optical microscopy. Selected whole-rock samples were broken into small chips and cleaned ultrasonically in distilled water containing <3% HNO_3 and washed with distilled water before being dried and handpicked to remove visible contamination. The rocks were powdered before analysis of major and trace elements, and Sr-Nd isotopes at SKLaBIG GIG CAS. Major-element oxides were determined by a Rigaku RIX 2000 X-ray fluorescence spectrometer on fused glass beads with analytical uncertainties <5% (Li et al., 2005). Trace elements were analyzed by a Perkin-Elmer Sciex ELAN 6000 instrument. Analytical procedures are the same as these described by Li et al. (2002). Trace element data of reference materials (BHVO-2, GSR-1, GSR-2, GSR-3, SARM-4, AGV-2, and W-2a) are given in Table S1.

Sr and Nd isotopic compositions of selected samples were determined using a MC-ICP-MS at SKLaBIG, GIG CAS. Analytical procedures are similar to those described in Wei et al. (2002) and Li et al. (2004). The $^{87}Sr/^{86}Sr$ ratio of the NBS987 standard and $^{143}Nd/^{144}Nd$ ratio of the Shin Etsu JNdi-1 standard measured were 0.710254 ± 11 (95%, n = 21) and 0.512099 ± 4 (95%, n = 15), respectively. All measured $^{143}Nd/^{144}Nd$ and $^{86}Sr/^{88}Sr$ ratios are fractionation corrected to $^{146}Nd/^{144}Nd$ = 0.7219 and $^{86}Sr/^{88}Sr$ = 0.1194, respectively. The BCR-2, JB-3, and JG-2 as three unknown samples yielded the $^{87}Sr/^{86}Sr$ and $^{143}Nd/^{144}Nd$ ratio were 0.703465 ± 11 (2σ, n = 3), 0.703448 ± 8, 0.758583 ± 13, and 0.512978 ± 5 (2σ, n = 3), 0.513052 ± 5, 0.512214 ± 4, respectively.

All zircon Hf isotope analyses in this study were performed on a Neptune Plus MC-ICP-MS (Thermo Scientific), coupled with a RESOlution M-50 193-nm laser ablation system (Resonetics), which are hosted at SKLaBIG, GIG CAS. The detailed description of the two instruments and data reduction procedure can be found in Zhang et al. (2014, 2015), respectively. Forty-seven analyses of the Plešovice zircon during the course of this study yielded a weighted mean of $^{176}Hf/^{177}Hf$ = 0.282486 ± 0.000005 (95%), which is consistent within errors with the reference value of 0.282483 ± 0.000013 in Sláma et al. (2008).

Measurements of zircon O isotopes were conducted using the Cameca IMS-1280 ion microprobe at IGG CAS. Analytical procedures are the same as those described by Li, Li, et al. (2010). Forty-seven measurements of the Penglai zircon standard during the course of this study yielded a weighted mean of $\delta^{18}O$ = 5.25 ± 0.19‰ (Table S2), which is identical within errors to the reported value of 5.31± 0.10‰ (Li, Long, et al., 2010).

4. Results

4.1. Zircon U-Pb Dating

Three amphibolite samples and three two-mica granite samples were selected for zircon dating. Zircons from mafic samples have crystal lengths of ~80–150 μm and length/width ratios from 1:1 to 2:1, while zircons from the granite samples have crystal lengths of ~150–300 μm and length/width ratios from 2:1 to 3:1. Zircon U-Pb isotopic data are given in Table S3. High Th/U ratios (0.08–1.03) of zircons from the Zhengga amphibolites and granites indicate a magmatic origin (Hoskin & Black, 2000). U-Pb spot analyses on samples 09TB78-3, 11SR02-4, and 16ML05-2 yielded $^{206}Pb/^{238}U$ data of 375 to 339 Ma (SIMS), 361 to 343 Ma (SIMS), and 363 to 358 Ma (LA-ICPMS), with weighted-mean ages of 359.4 ± 4.2 Ma (MSWD = 2.6), 353.0 ± 2.9 Ma (MSWD = 1.6), and 361.6 ± 3.3 Ma (MSWD = 0.06), respectively, for the three amphibolite samples (Figures 4a–4c and Table S3). SIMS U-Pb dating on samples 09TB78-2, 11SR02-1, and 11SR02-3

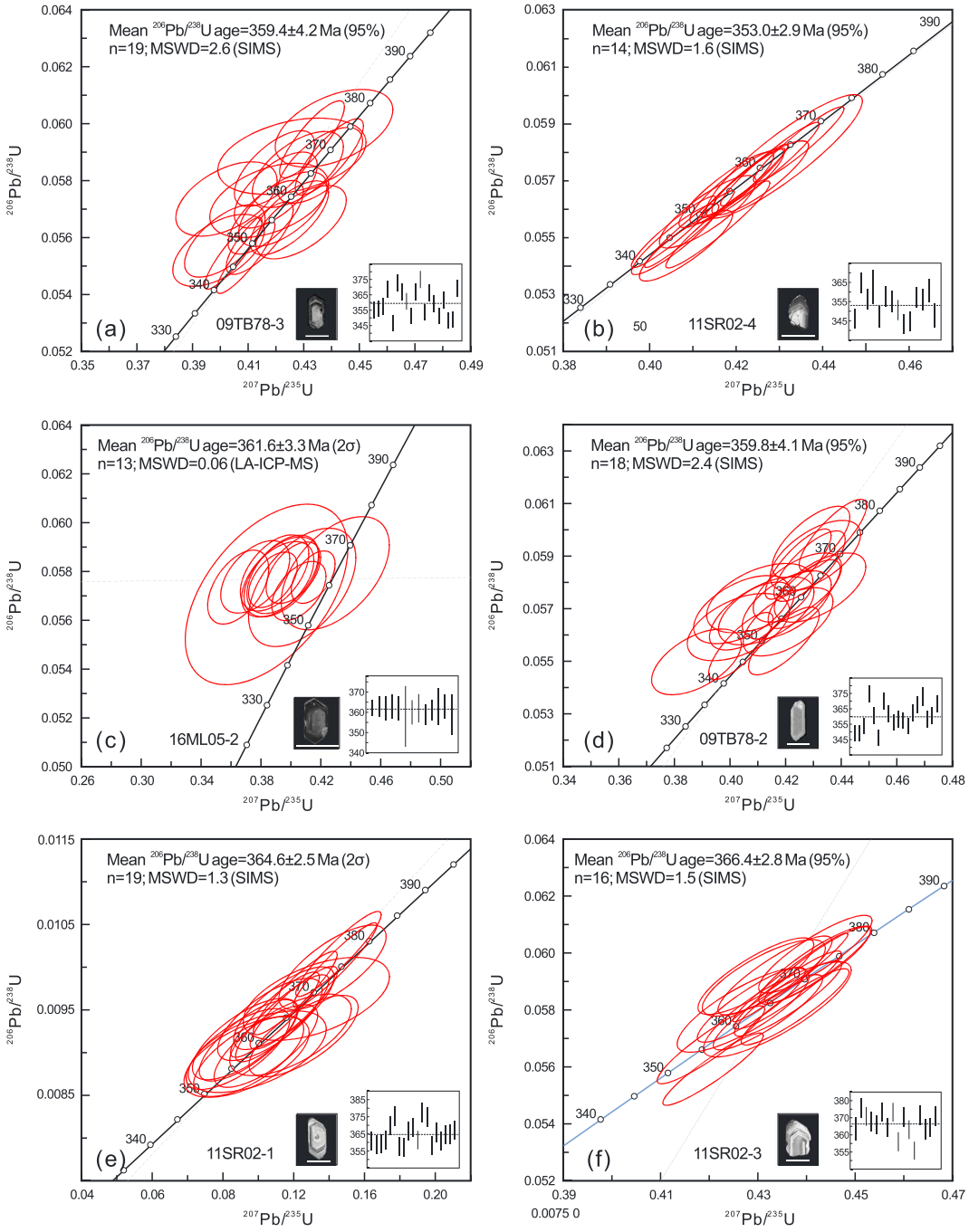

Figure 4. SIMS and LA-ICP-MS zircon U-Pb concordia diagrams with cathodoluminescence images for (a) 09TB78-3, (b) 11SR02-4 and (c) 16ML05-2 (amphibolite), and (d) 09TB78-2; (e) 11SR02-1, and (f) 11SR02-3 (two-mica granite). SIMS = secondary ion mass spectrometer; LA-ICP-MS = Laser ablation inductively coupled plasma mass spectrometer.

yielded $^{206}Pb/^{238}U$ data of 374 to 350 Ma, 388 to 357 Ma, and 387 to 351 Ma, with weighted-mean ages of 359.8 ± 4.1 Ma (MSWD = 2.4), 364.6 ± 2.5 Ma (MSWD = 1.3), and 366.4 ± 2.8 Ma (MSWD = 1.5), respectively for the three two-mica granites samples (Figures 4d–4f and Table S3). With exception of a younger date of 353 Ma for the amphibolite enclave sample (11SR02-4), the other amphibolite and two-mica granite samples show relatively consistent zircon U-Pb ages ranging from 366.4 to 359.4 Ma, indicating that the Zhengga two-mica granites and amphibolites were emplaced in the Late Devonian-Early Carboniferous.

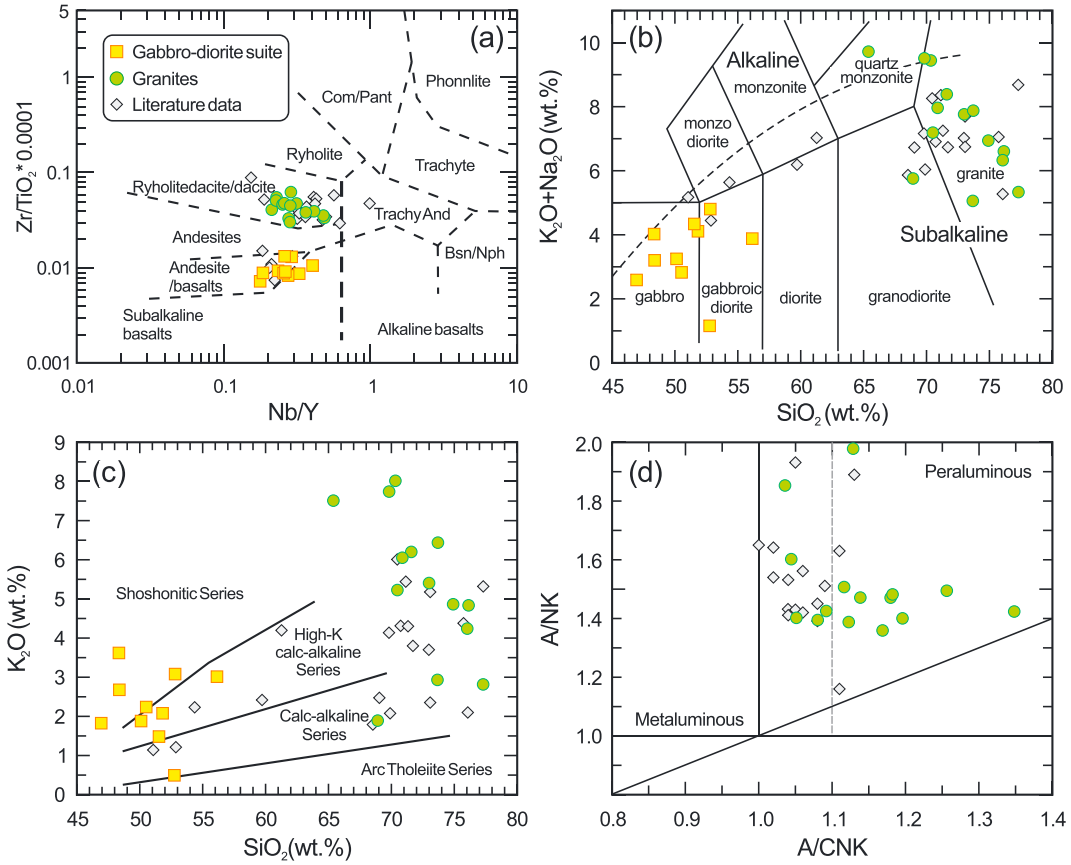

Figure 5. (a) Nb/Y versus Zr/TiO_2 (after Winchester & Floyd, 1977). (b) SiO_2 versus Na_2O+K_2O classification diagram (after Middlemost, 1994). (c) SiO_2 versus K_2O plot (after Peccerillo & Taylor, 1976). (d) A/CNK versuss A/NK classification diagram. The literature data are from Dong et al. (2014) and Ji et al. (2012).

4.2. Major and Trace Elements

The Late Paleozoic Zhengga intrusive rocks can be subdivided into a mafic group and a felsic group (Figure 5 and Table 1). The mafic rocks have low SiO_2 (47.0–56.2 wt.%), Al_2O_3 (10.2–16.2 wt.%), and high MgO (6.8–12.9 wt.%) and plot in the subalkalic basalt field on the Zr/TiO_2 versus Nb/Y diagram (Figure 5). This group are similar in composition to high-MgO basalt, which is defined as having $SiO_2 \leq 54$ wt.%, MgO ≥ 7 wt.%, and $Al_2O_3 < 16.5$ wt.% (Kersting & Arculus, 1994; Pichavant et al., 2002). The Zhengga felsic rocks have high SiO_2 (65.4–77.3 wt.%), Al_2O_3 (11.5–17.3 wt.%), and low MgO (0.5–1.4 wt.%) and CaO contents with high and variable A/CNK ratios (1.04–1.35; Figure 5).

With the exception of samples 09TB78-3 and 16ZG02-3 that have high total rare earth element (∑REE) contents (175 and 178 ppm, respectively), the Zhengga mafic rocks have relatively low ∑REE contents (28–97 ppm) in comparison to the felsic rocks with ∑REE contents of 134–265 ppm. Chondrite-normalized REE patterns show that the mafic rocks are characterized by slightly to moderately enriched light REE ($(La/Sm)_{CN}$ = 1.9–3.9) and relatively flat heavy REE ($(Dy/Yb)_{CN}$ = 1.2–1.7) patterns without marked Eu anomalies ($Eu/Eu^* = Eu_{CN}/(Sm_{CN} \times Gd_{CN})^{1/2}$ = 0.83–1.26) (Figure 6a). The felsic rocks are moderately enriched in LREEs ($(La/Sm)_{CN}$ = 2.9–4.6), with flat Heavy (H)REE patterns ($(Dy/Yb)_{CN}$ = 1.2–1.7), pronounced negative Eu anomalies (Eu/Eu* ratios from 0.25 to 0.87; Figure 6b).

On normal mid-ocean ridge basalt (N-MORB) normalized plots, the Zhengga mafic rock samples are markedly enriched in many of the most incompatible elements including Th, U, and Rb and are slightly depleted in Zr, Hf, and Ti with marked negative Nb and Ta anomalies (Figure 6c). In addition, the mafic rocks have high Cr (400–1526 ppm) and Ni (167–352 ppm) contents. The Zhengga felsic rocks are also enriched in Th, U, and Rb and possess significant negative Nb, Sr and Ti anomalies (Figure 6d).

Journal of Geophysical Research: Solid Earth
10.1029/2018JB017106

Table 1
Major (wt.%) and Trace (ppm) Elements Data of Neopaleozoic Zhengga Magmatic Rocks

	Sample No.											
	09TB78-3	11SR02-2	11SR02-4	16ML05-1	16ML05-2	16ML05-3	16ZG02-2	16ZG02-3	16ZG02-4	16ZG03-2	09TB78-2	11SR02-1
	Rock Type											
	Amphibolite	Mafic enclave	Mafic enclave	Mafic enclave	Mafic enclave	Mafic enclave	Amphibolite	Amphibolite	Amphibolite	Amphibolite	Gneissose granite	Two-mica granite
	Latitude											
	29°16′32″	29°15′54″	29°15′54″	29°15′54″	29°15′54″	29°15′54″	29°16′32.3″	29°16′32.3″	29°16′32.3″	29°16′32.4″	29°16′32″	29°15′54″
	Longitude											
Elements	92°10′01″	92°10′33″	92°10′33″	92°10′33″	92°10′33″	92°10′33″	92°09′59.5″	92°09′59.5″	92°09′59.5″	92°10′00.2″	92°10′01″	92°10′33″
SiO_2	50.12	48.39	48.35	52.76	50.53	56.15	52.82	51.82	46.95	51.54	71.61	73.71
TiO_2	0.78	0.90	0.88	0.84	0.62	0.87	0.70	0.67	0.91	0.84	0.35	0.28
Al_2O_3	13.08	14.01	12.22	13.54	10.19	13.62	16.15	14.37	13.03	15.54	14.29	13.82
$Fe_2O_3^T$	7.86	10.81	10.05	9.17	9.93	7.21	7.76	8.09	12.05	7.64	2.07	1.84
MnO	0.15	0.25	0.22	0.27	0.24	0.19	0.13	0.15	0.18	0.13	0.03	0.03
MgO	12.18	10.14	12.93	8.39	12.62	6.82	9.06	10.23	11.05	9.00	0.76	0.84
CaO	10.45	10.13	8.37	12.89	10.34	9.66	7.68	9.40	11.78	8.36	1.34	1.30
Na_2O	1.37	0.52	0.40	0.66	0.58	0.86	1.72	2.03	0.76	2.85	2.18	1.43
K_2O	1.88	2.68	3.62	0.49	2.24	3.01	3.08	2.07	1.82	1.48	6.20	6.44
P_2O_5	0.38	0.18	0.15	0.18	0.13	0.20	0.16	0.28	0.25	0.34	0.13	0.12
L.O.I	1.20	1.18	1.97	0.77	2.47	1.34	0.65	0.82	0.72	1.81	0.74	0.64
Total	99.45	99.17	99.16	99.96	99.90	99.93	99.92	99.94	99.50	99.55	99.70	100.45
A/CNK											1.12	1.18
$Mg^{\#}$	75.4	65.0	71.8	64.4	71.6	65.2	69.8	71.5	64.5	70.0	42.2	47.5
Sc	22.4	28.4	29.8	29.5	26.6	27.7	22.6	25.1	37.5	19.3	4.78	5.49
V	172	181	219	183	196	174	181	198	276	155	31.5	26.8
Cr	698	752	912	728	894	624	477	671	1526	400	9.77	110
Ni	281	263	352	167	289	138	185	187	169	237	4.37	11.0
Ga	15.6	15.8	15.4	17.2	12.7	13.7	17.0	15.6	18.4	16.1	15.7	15.1
Rb	84.2	186	306	25.3	177	240	196	98.8	101	66.9	172	209
Sr	461	246	147	252	219	406	447	769	311	666	130	142
Y	15.9	19.1	14.7	25.3	14.9	16.8	13.4	17.9	19.2	16.0	38.2	36.4
Zr	82.3	64.2	72.6	73.2	57.1	75.2	90.5	87.4	79.8	76.5	104	91.6
Nb	6.42	3.40	4.05	6.50	3.51	5.53	3.92	4.67	3.57	4.24	10.8	10.1
Cs	6.13	10.2	10.9	6.88	4.78	4.97	15.7	8.88	8.11	4.31	5.96	3.39
Ba	235	179	484	34.9	203	238	407	528	359	219	654	617
La	34.6	10.3	7.94	13.0	10.6	11.1	11.4	35.8	11.5	16.7	38.2	25.1
Ce	73.9	23.1	18.3	32.6	24.1	24.3	24.9	75.5	25.6	36.6	76.8	52.4
Pr	8.88	3.29	2.65	4.31	3.23	3.19	3.23	9.34	3.42	5.00	8.90	6.36
Nd	36.7	14.8	11.7	17.1	13.2	13.6	13.9	36.9	15.5	21.8	32.0	22.8
Sm	6.71	3.34	2.77	3.81	2.79	2.97	2.80	5.90	3.68	4.31	6.96	4.90
Eu	1.88	0.91	0.94	1.23	1.12	1.05	0.92	1.43	1.04	1.29	0.86	0.79
Gd	4.90	3.36	2.83	3.63	2.64	2.83	2.64	4.69	3.70	3.70	6.61	5.13
Tb	0.64	0.56	0.45	0.66	0.43	0.48	0.39	0.59	0.57	0.52	1.21	0.92
Dy	3.30	3.43	2.71	4.30	2.70	3.03	2.38	3.21	3.37	2.88	7.02	5.95
Ho	0.60	0.74	0.56	0.91	0.57	0.64	0.49	0.64	0.69	0.58	1.43	1.33

Journal of Geophysical Research: Solid Earth

10.1029/2018JB017106

Table 1
(continued)

	Sample No.											
	09TB78-3	11SR02-2	11SR02-4	16ML05-1	16ML05-2	16ML05-3	16ZG02-2	16ZG02-3	16ZG02-4	16ZG03-2	09TB78-2	11SR02-1
	Rock Type											
	Amphibolite	Mafic enclave	Mafic enclave	Mafic enclave	Mafic enclave	Mafic enclave	Amphibolite	Amphibolite	Amphibolite	Amphibolite	Gneissose granite	Two-mica granite
	Latitude											
	29°16′32″	29°15′54″	29°15′54″	29°15′54″	29°15′54″	29°15′54″	29°16′32.3″	29°16′32.3″	29°16′32.3″	29°16′32.4″	29°16′32″	29°15′54″
	Longitude											
Elements	92°10′01″	92°10′33″	92°10′33″	92°10′33″	92°10′33″	92°10′33″	92°09′59.5″	92°09′59.5″	92°09′59.5″	92°10′00.2″	92°10′01″	92°10′33″
Er	1.54	1.99	1.50	2.43	1.46	1.68	1.31	1.64	1.81	1.50	3.78	3.80
Tm	0.21	0.29	0.21	0.38	0.22	0.25	0.18	0.23	0.26	0.21	0.52	0.56
Yb	1.32	1.92	1.47	2.48	1.40	1.59	1.21	1.48	1.68	1.35	3.14	3.48
Lu	0.20	0.30	0.24	0.40	0.22	0.25	0.18	0.23	0.25	0.20	0.45	0.52
Hf	2.38	1.63	1.78	2.05	1.62	2.08	2.41	2.42	2.43	1.94	3.30	2.74
Ta	0.39	0.22	0.24	0.34	0.25	0.33	0.23	0.28	0.24	0.24	0.73	0.73
Pb	8.82	2.11	1.84	3.21	2.26	3.51	11.23	14.43	8.98	7.54	30.5	43.7
Th	5.13	1.44	1.21	2.55	1.41	2.11	1.81	6.79	3.74	1.78	17.1	12.3
U	1.79	0.86	0.87	3.81	0.79	2.60	0.58	1.49	1.10	0.59	1.66	1.86
T_{Zr} (°C)											707.1	705.8
T_{LREE} (°C)											717.3	700.8

	Sample No.											
	11SR02-3	16ML04-1	16ML04-2	16ML04-3	16ML04-4	16ML05-4	16ZG01-1	16ZG01-2	16ZG01-3	16ZG02-1	16ZG03-1	16ML13-2
	Rock Type											
	Two-mica granite	Two-mica granite	Two-mica granite	Two-mica granite	Two-mica granite	Two-mica granite	Gneissose granite	Gneissose granite	Gneissose granite	Gneissose granite	Gneissose granite	Gneissose granite
	Latitude											
	29°15′54″	29°15′54″	29°15′54″	29°15′54″	29°15′54″	29°15′54″	29°16′32″	29°16′32″	29°16′32″	29°16′32″	29°16′32″	29°16′32″
	Longitude											
Elements	92°10′33″	92°10′33″	92°10′33″	92°10′33″	92°10′33″	92°10′33″	92°10′0.1″	92°10′0.1″	92°10′0.1″	92°10′00″	92°10′00″	92°10′00″
SiO_2	69.84	77.32	74.92	70.50	76.15	70.34	73.68	70.89	76.05	68.93	73.00	65.40
TiO_2	0.28	0.21	0.25	0.22	0.22	0.37	0.36	0.43	0.27	0.41	0.33	0.43
Al_2O_3	15.80	11.50	12.16	12.66	11.98	14.97	13.18	14.48	12.09	15.57	13.83	17.29
$Fe_2O_3^T$	2.07	2.39	2.70	2.51	2.27	2.18	2.66	2.51	2.02	3.10	2.22	3.36
MnO	0.03	0.09	0.09	0.06	0.05	0.05	0.06	0.04	0.03	0.04	0.02	0.09
MgO	0.88	0.47	0.55	0.57	0.60	0.74	1.03	0.98	0.73	1.35	0.84	0.89
CaO	1.06	2.11	1.59	1.49	1.31	0.99	2.76	1.01	1.54	3.64	0.30	1.60
Na_2O	1.77	2.52	2.07	1.96	1.77	1.42	2.12	1.91	2.09	3.86	2.35	2.21
K_2O	7.74	2.81	4.86	5.22	4.83	8.01	2.93	6.05	4.24	1.89	5.41	7.51

Journal of Geophysical Research: Solid Earth

10.1029/2018JB017106

Table 1
(continued)

	Sample No.											
	09TB78-3	11SR02-2	11SR02-4	16ML05-1	16ML05-2	16ML05-3	16ZG02-2	16ZG02-3	16ZG02-4	16ZG03-2	09TB78-2	11SR02-1
	Rock Type											
	Amphibolite	Mafic enclave	Mafic enclave	Mafic enclave	Mafic enclave	Mafic enclave	Amphibolite	Amphibolite	Amphibolite	Amphibolite	Gneissose granite	Two-mica granite
	Latitude											
	29°16′32″	29°15′54″	29°15′54″	29°15′54″	29°15′54″	29°15′54″	29°16′32.3″	29°16′32.3″	29°16′32.3″	29°16′32.4″	29°16′32″	29°15′54″
	Longitude											
Elements	92°10′01″	92°10′33″	92°10′33″	92°10′33″	92°10′33″	92°10′33″	92°09′59.5″	92°09′59.5″	92°09′59.5″	92°10′00.2″	92°10′01″	92°10′33″
P_2O_5	0.12	0.11	0.12	0.12	0.12	0.15	0.12	0.10	0.14	0.11	0.12	0.15
L.O.I	0.72	0.45	0.63	4.39	0.65	0.73	0.57	0.92	0.41	0.55	1.17	0.68
Total	100.30	99.97	99.95	99.70	99.95	99.95	99.46	99.32	99.60	99.45	99.57	99.60
A/CNK	1.20	1.04	1.05	1.09	1.14	1.17	1.13	1.26	1.12	1.04	1.35	1.18
$Mg^{\#}$	45.6	28.0	28.6	31.0	34.5	40.2	43.5	43.6	41.8	46.3	42.7	34.4
Sc	5.68	4.37	5.01	4.82	4.52	5.91	6.13	7.57	5.02	6.00	6.11	7.45
V	27.6	14.2	15.3	16.7	13.7	25.7	34.1	38.2	23.6	47.5	32.2	34.3
Cr	90.6	13.1	82.5	28.2	17.6	16.6	11.0	11.1	8.0	20.4	11.6	41.3
Ni	8.03	5.25	5.27	3.94	3.27	3.73	5.46	5.54	3.96	9.50	5.12	8.53
Ga	17.3	14.4	15.0	16.6	15.2	18.3	17.0	17.0	14.9	18.2	17.5	22.5
Rb	254	118	187	210	192	246	141	207	163	78.1	176	275
Sr	131	66.6	72.8	75.5	65.4	115.2	88.5	97.0	84.1	511.1	76.1	157
Y	31.8	46.8	47.4	50.6	44.8	64.8	40.4	38.4	45.8	23.2	31.9	61.7
Zr	176	84.5	117	114	117	166	167	142	124	159	124	157
Nb	9.16	10.0	12.3	11.5	10.3	18.5	12.8	18.7	11.6	9.6	11.6	18.2
Cs	3.86	2.51	3.15	3.30	3.18	3.43	5.58	5.44	4.09	6.65	2.05	6.22
Ba	841	188	305	350	313	696	462	723	471	511	722	1197
La	29.4	27.3	29.0	27.7	31.2	50.2	42.2	47.9	34.2	36.9	39.5	49.0
Ce	60.9	59.9	64.1	61.0	69.3	109.2	87.3	98.1	71.2	74.3	86.4	102
Pr	7.16	7.11	7.61	7.21	8.13	12.8	10.3	11.6	8.46	8.28	9.84	11.8
Nd	26.4	25.3	27.5	25.9	28.9	45.4	38.0	42.9	31.4	30.3	37.7	42.7
Sm	5.40	5.82	6.26	5.93	6.47	9.22	7.13	8.14	6.53	5.23	7.15	8.10
Eu	0.92	0.49	0.50	0.53	0.48	0.98	0.87	0.95	0.68	1.40	0.79	1.28
Gd	5.18	5.74	6.03	5.86	6.17	8.59	6.66	7.29	6.42	4.61	6.46	7.47
Tb	0.88	1.18	1.22	1.23	1.21	1.57	1.07	1.13	1.13	0.67	1.01	1.40
Dy	5.55	7.98	8.01	8.36	7.81	10.45	6.64	6.54	7.16	3.87	5.76	9.71
Ho	1.19	1.65	1.65	1.75	1.57	2.32	1.35	1.30	1.51	0.78	1.12	2.18
Er	3.24	4.18	4.12	4.41	3.92	6.36	3.57	3.29	4.03	2.08	2.86	6.08
Tm	0.48	0.59	0.59	0.63	0.55	0.96	0.50	0.46	0.59	0.31	0.38	0.95
Yb	3.04	3.35	3.35	3.54	3.09	5.78	3.14	2.78	3.54	2.05	2.38	5.94
Lu	0.46	0.46	0.46	0.50	0.44	0.87	0.45	0.40	0.51	0.31	0.33	0.89
Hf	5.01	3.09	3.96	3.98	4.03	5.25	5.15	4.35	3.89	4.83	3.93	4.92
Ta	0.56	0.60	0.76	0.74	0.63	1.32	0.87	1.22	0.85	0.87	0.77	1.56
Pb	53.6	29.4	40.0	42.6	36.7	50.8	18.0	37.2	24.8	22.8	22.6	45.8
Th	14.7	15.6	18.6	17.6	20.7	26.3	20.1	23.9	16.2	14.7	21.0	25.2

Table 1
(continued)

	Sample No.										
	09TB78-3	11SR02-2	11SR02-4	16ML05-1	16ML05-2	16ML05-3	16ZG02-2	16ZG02-3	16ZG02-4	16ZG03-2	09TB78-2	11SR02-1
	Rock Type											
	Amphibolite	Mafic enclave	Mafic enclave	Mafic enclave	Mafic enclave	Mafic enclave	Amphibolite	Amphibolite	Amphibolite	Amphibolite	Gneissose granite	Two-mica granite
	Latitude											
	29°16′32″	29°15′54″	29°15′54″	29°15′54″	29°15′54″	29°15′54″	29°16′32.3″	29°16′32.3″	29°16′32.3″	29°16′32.4″	29°16′32″	29°15′54″
	Longitude											
Elements	92°10′01″	92°10′33″	92°10′33″	92°10′33″	92°10′33″	92°10′33″	92°09′59.5″	92°09′59.5″	92°09′59.5″	92°10′00.2″	92°10′01″	92°10′33″
U	1.98	2.47	2.70	2.71	2.72	3.27	3.92	2.02	2.11	2.34	2.37	3.36
T_{Zr} (°C)	764.5	689.2	716.5	715.6	730.6	756.7	761.0	753.6	732.8	728.6	753.1	740.3
T_{LREE} (°C)	713.4	682.0	692.3	655.1	713.2	753.3	704.3	751.5	715.1	669.0	759.8	736.7

Note. $Fe_2O_3^T$ = total Fe_2O_3 content; $Mg^{\#}$ = molecular $Mg^{2+}/(Mg^{2+}+Fe^{2+}) \times 100$; A/CNK = molecular $Al_2O_3/(CaO+Na_2O+K_2O)$; T_{Zr} are calculated after Boehnke et al. (2013). T_{LREE} are calculated after Montel (1993).

4.3. Sr-Nd-Hf-O Isotopes

In this study, initial Sr-Nd isotopic ratios of the Zhengga granite and literature data were calculated using a weighted mean formation age of 361.5 Ma. The Zhengga mafic and felsic rocks exhibit very different bulk rock Nd isotopic signatures (Table 2). The mafic rocks have variable positive $\varepsilon_{Nd}(t)$ values (+3.3 to +8.0) with Nd isotope model ages (T_{DM}) ranging from 454 to 946 Ma, while the felsic rocks show negative and relatively uniform $\varepsilon_{Nd}(t)$ values (−7.8 to −8.6) with Nd isotope model ages (T_{DM}) ranging from 2.10 to 1.83 Ga (Figure 7 and Table 2). Except for one mafic sample (11SR02-4) that has high Rb content (306 ppm) with very low initial $^{87}Sr/^{86}Sr$ ratios of 0.6889, the Zhengga mafic and felsic rocks both have variable initial $^{87}Sr/^{86}Sr$ ratios (0.7054–0.7173 and 0.7030–0.7374, respectively; Figure 7 and Table 2). The low initial $^{87}Sr/^{86}Sr$ calculated for 11SR02-4 is due to the addition of Rb during subsolidus alteration. This is confirmed by the recalculation of the initial $^{87}Sr/^{86}Sr$ for sample 11SR02-4 using the average of the Rb content in the rest of the mafic samples (128 ppm), which yields a more realistic initial $^{87}Sr/^{86}Sr$ ratio of 0.7070.

The zircon Hf-O isotopic data for the Zhengga mafic (09TB78-3) and granite sample (09TB78-2, 11SR02-1, and 11SR02-3) are given in Table S2. Zircon analyses from the amphibolite have consistent initial $^{176}Hf/^{177}Hf$ ratios, ranging from 0.282560 to 0.282865, and positive $\varepsilon_{Hf}(t)$ values of +0.4 to +11.2, with model ages T_{DM} of 978 to 547 Ma (Figure 7b). Zircon analyses from three granite samples have variable initial $^{176}Hf/^{177}Hf$ ratios (0.282266 to 0.282533), negative $\varepsilon_{Hf}(t)$ values (−10.4 to −1.3), and model ages T_{DM} of 1423 to 1054 Ma (Figure 7b). The analyzed igneous zircons of mafic rocks show relatively low, but variable, $\delta^{18}O$ values (4.59–7.76‰) with an average value of 5.72 ± 0.18‰ similar to those (5.3 ± 0.3‰) of igneous zircons in equilibrium with mantle magmas (Valley et al., 2005), whereas the granites have high zircon $\delta^{18}O$ values of 9.45 ± 0.2‰.

5. Discussion

5.1. Petrogenesis of Zhengga Mafic Rocks

5.1.1. Effects of Alteration and Metamorphism

Petrographic observations show that the studied Zhengga mafic samples have experienced varying degrees of alteration, up to greenschist facies metamorphism, as indicated by the presence of epidote (Figure 3). It is therefore important to evaluate the elemental effects of alteration and low-grade metamorphism before using the geochemistry to interpret their tectonic settings.

Correlations between other elements and a known immobile element (Zr in this study) can be used to assess the mobility of elements (e.g., Hastie et al., 2013). With the exception of the alkali metals (such as Rb and K), most other large ion lithophile elements (such as Na, Mg, Ca, Sr, and Ba), high-field strength elements (HFSEs; such as Nb, Ta, Th, and Hf), REEs, and Y all show good correlations with Zr (Figure S2). This indicates that these elements were relatively immobile during metamorphism and alteration (cf. Hastie et al., 2013). These are consistent with studies that show that the REEs and HFSEs as well as Th and Ti are generally relatively immobile in igneous rocks during alteration and low-grade metamorphism (Hastie et al., 2007).

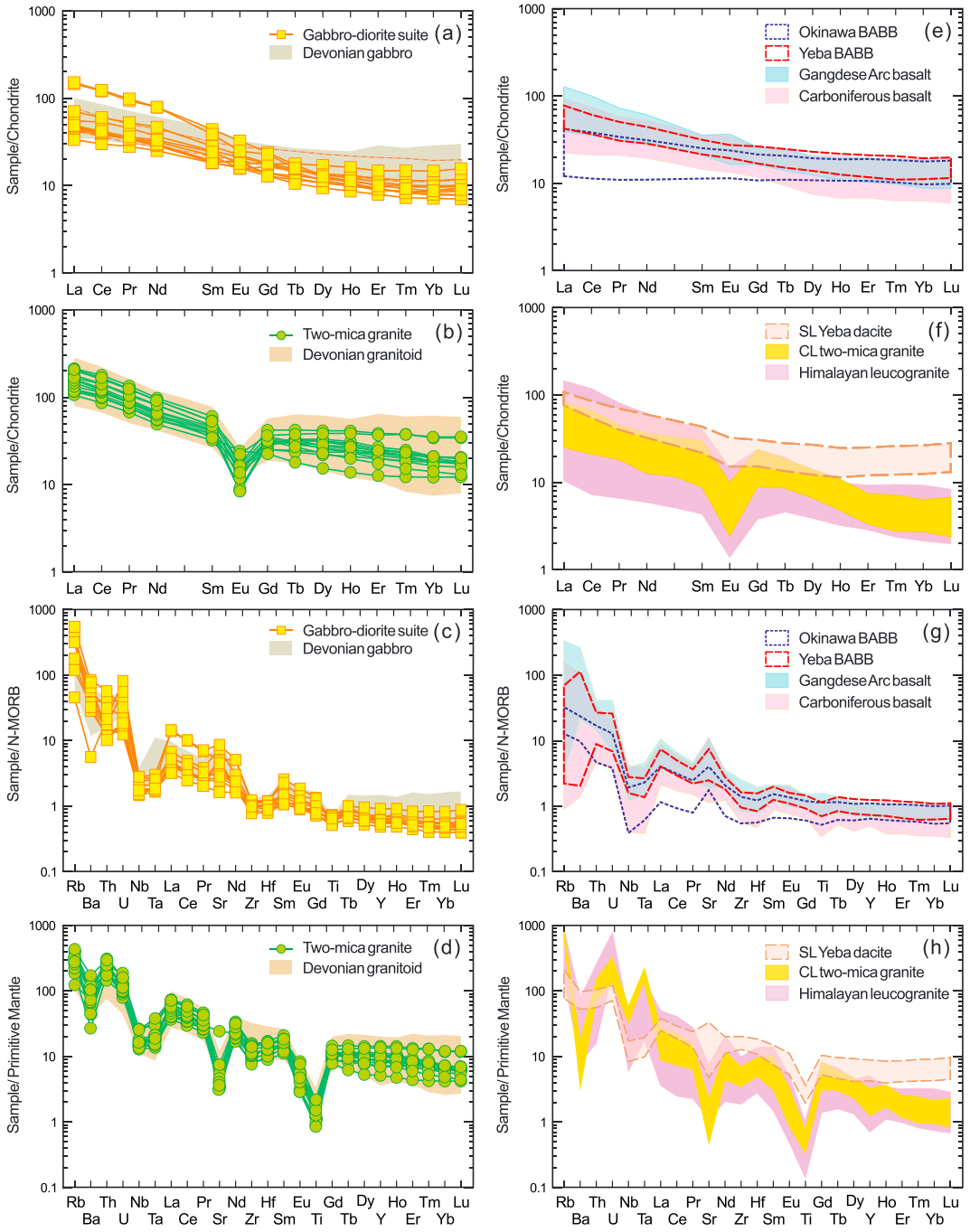

Figure 6. Chondrite-normalized rare earth element patterns for the Zhengga mafic rocks (a) with other back-arc and arc basalts (e) and the Zhengga silicic rocks (b) with other granites in southern Tibet (f); N-MORB-normalized multielement diagram for the Zhengga mafic rocks (c) with other back-arc and arc basalts (g); primitive mantle-normalized multielement diagram for the Zhengga silicic rocks (d) with other granites in southern Tibet (h). Data of the Gangdese arc basalts are from Kang et al. (2014), Wang et al. (2016), and Zhu et al. (2008); Okinawa Trough back-arc basin basalts (BABBs) are from Shinjo and Kato (2000). Devonian mafic rocks are from Dong et al. (2014). Carboniferous basalts are from Zhu et al. (2010). Yeba BABBs and dacites are from Wei et al. (2017). Devonian granites are from Dong et al. (2014) and Ji et al. (2012). Himalayan leucogranite are form Guo and Wilson (2012). CL two-mica granites are from Liu et al. (2006). The values of chondrite, primitive mantle and N-MORB are from Sun and McDonough (1989). Abreviations: CL = central Lhasa. SL = southern Lhasa. N-MORB = normal mid-ocean ridge basalt.

Table 2
Sr and Nd Isotope Data for the Zhengga Magmatic Rocks

Sample	Rb (ppm)	Sr (ppm)	$^{87}Rb/^{86}Sr$	$^{87}Sr/^{86}Sr \pm 2\sigma$	$(^{87}Sr/^{86}Sr)_i$	Sm (ppm)	Nd (ppm)	$^{147}Sm/^{144}Nd$	$^{143}Nd/^{144}Nd \pm 2\sigma$	$(^{143}Nd/^{144}Nd)_i$	$\varepsilon_{Nd}(t)$	T_{DM} (Ma)	T^2_{DM} (Ma)
09TB78-3	84.2	461	0.5284	0.711206±7	0.708487	6.71	36.69	0.1104	0.512845±2	0.5126	8.02	454	
11SR02-2	186	246	2.1916	0.719850±5	0.708570	3.34	14.80	0.1365	0.512765±4	0.5124	5.25	766	
11SR02-4	306	147	6.0268	0.719953±5	0.688936	2.77	11.70	0.1431	0.512801±4	0.5125	5.66	758	
16ML05-1	25.3	252	0.2900	0.718786±12	0.717293	3.81	17.13	0.1342	0.512659±6	0.5123	3.30	946	
16ML05-2	177	219	2.3346	0.719687±9	0.707672	2.79	13.24	0.1273	0.512796±7	0.5125	6.30	628	
16ML05-3	240	406	1.7122	0.718405±13	0.709593	2.97	13.59	0.1318	0.512822±7	0.5125	6.60	614	
16ZG02-3	98.8	769	0.3716	0.708439±7	0.706526	5.90	36.88	0.0966	0.512573±5	0.5123	3.37	754	
16ZG03-2	66.9	666	0.2908	0.706855±9	0.705358	4.31	21.75	0.1197	0.512804±5	0.5125	6.79	565	
09TB78-2	172	130	3.8141	0.756998±6	0.737369	6.96	31.96	0.1315	0.512057±3	0.5117	−8.33	2028	1792
11SR02-1	209	142	4.2421	0.727320±8	0.705488	4.90	22.79	0.1299	0.512039±3	0.5117	−8.61	2020	1814
11SR02-3	254	131	5.5973	0.732303±8	0.703496	5.40	26.38	0.1238	0.512044±3	0.5118	−8.22	1874	1783
16ML04-2	187	72.8	7.4196	0.753527±10	0.715342	6.26	27.51	0.1375	0.512100±5	0.5118	−7.78	2102	1746
16ML05-4	246	115	6.1838	0.734791±10	0.702966	9.22	45.44	0.1226	0.512059±6	0.5118	−7.88	1827	1756
16ZG01-1	141	88.5	4.6299	0.753477±10	0.729649	7.13	38.00	0.1134	0.512072±6	0.5118	−7.21	1640	1702
16ZG02-1	78.1	511	0.4428	0.722204±9	0.719926	5.23	30.34	0.1041	0.512075±6	0.5118	−6.72	1497	1663
16ZG03-1	176	76.1	6.7130	0.746234±10	0.711686	7.15	37.67	0.1147	0.512074±5	0.5118	−7.22	1657	1702

Note. The groups are same as Table 1 (details see text). $\varepsilon_{Nd}(t) = [(^{143}Nd/^{144}Nd)_S/(^{143}Nd/^{144}Nd)_{CHUR} - 1] \times 10{,}000$. $TDM = \ln[(^{143}Nd/^{144}Nd)_S - (^{143}Nd/^{144}Nd)DM]/[(^{143}Sm/^{144}Nd)_S - (^{147}Sm/^{144}Nd)_{DM}/\lambda$ (DePaolo, 1998). In the calculation $(^{143}Nd/^{144}Nd)_{CHUR} = 0.512638$ $(^{147}Sm/^{144}Nd)_{CHUR} = 0.1967$ $(^{143}Nd/^{144}Nd)_{DM} = 0.51315$, $(^{147}Sm/^{144}Nd)_{DM} = 0.2136$ and $t = 361.5$ Ma.

5.1.2. Crustal Contamination

Crustal contamination is almost inevitable for mantle-derived melts during their ascent through continental crust or their evolution within crustal magma chambers (e.g., Castillo et al., 1999). The slightly variable Nd isotope characteristics and depleted Nb-Ta anomalies of the Zhengga mafic rocks could possibly be the result of crustal contamination during magma ascent. Given that crustal components generally contain distinctly low $\varepsilon_{Nd}(t)$, MgO, low $(Nb/La)_{PM}$, and Nb/Th values and high $^{87}Sr/^{86}Sr$ ratios (Rudnick & Fountain, 1995), any crustal contamination that occurred during magma ascent would have caused an increase in $(^{87}Sr/^{86}Sr)_i$ and a decrease in $\varepsilon_{Nd}(t)$ with increasing SiO_2 in the magma suites (e.g., Rogers et al., 2000). However, such a compositional trend has not been observed for the Zhengga mafic rocks (Figure 7), suggesting that minimal crustal contamination occurred during the formation of these rocks. Moreover, the vast majority of the Zhengga mafic rocks show a small range in initial $^{143}Nd/^{144}Nd$ ratios (0.5123–0.5126) and high and positive $\varepsilon_{Nd}(t)$ (+3.3 to +8.0; Table 2), which also are inconsistent with significant crustal contamination.

5.1.3. Mantle Source and Petrogenesis

The Zhengga mafic rocks possess low SiO_2, Al_2O_3, and high MgO, Cr, and Ni contents with high positive $\varepsilon_{Nd}(t)$ and $\varepsilon_{Hf}(t)$ values, suggesting they are derived from a depleted mantle source. The Late Paleozoic mafic rocks from the Zhengga area exhibit marked negative Nb-Ta-Ti anomalies on primitive mantle-normalized incompatible trace element diagrams (Figure 6c), indicating that they are unlikely to be derived from normal MORB- or OIB-source mantle (e.g., Hofmann, 1997).

Subduction-related magmas are characterized by significant enrichment in large ion lithophile elements (Rb, Ba, and Sr) and light (L) REE relative to the HFSE (Nb, Ta, Zr, and Hf) and HREE, with significant negative Nb-Ta-Ti anomalies on N-MORB-normalized multielement diagrams (e.g., Pearce et al., 2005). These characteristics are also shown by the Late Paleozoic mafic rocks from the Zhengga area (Figure 6c), and so these rocks are likely to have formed in a subduction-related setting.

The Zhengga mafic magmas therefore were most probably derived from a mantle source metasomatized, or enriched, by fluids or melts derived from subducted oceanic slabs comprising basaltic crust and sediment. Previous studies have shown that slab-derived fluids have high contents of Ba, Sr, U, and Pb (e.g., Elliott, 2003), whereas subducted oceanic sediment-derived melts contain high concentrations of both Th and LREE contents, but with distinctly elevated Th/La and Th/Ce ratios (e.g., Hastie et al., 2013; Plank, 2005). This is because Th is a strongly incompatible element and is abundant in sediments and the middle-upper crust (e.g.,Plank, 2005; Rudnick & Gao, 2014).

The Zhengga mafic rocks possess low Sr/Th (mean 165), which are inconsistent with the fluid-induced enrichment (Figure 8d). In contrast, relatively high Th/La ratios of the Zhengga mafic rocks (mean 0.17) lie between that of N-MORB (Th/La = 0.05) and marine sediments (Th/La = 0.2) and suggest potential involvement of sediment-derived melts in the generation of the Zhengga mafic rocks. The Zhengga mafic rocks have Th contents ranging from 1.2 to 6.8 ppm

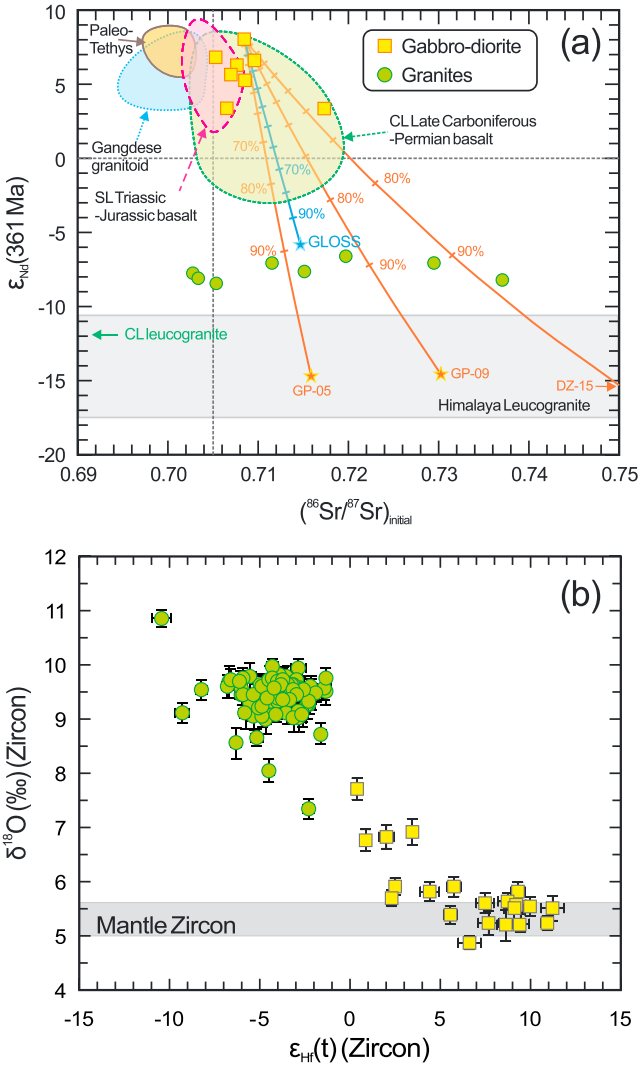

Figure 7. (a) $\varepsilon_{Nd}(t)$ versus $(^{87}Sr/^{86}Sr)_i$ and (b) zircon $\varepsilon_{Hf}(t)$ versus $\delta^{18}O$ diagrams for the Zhengga magmatic rocks. Data sources: Paleo-Tethyan ophiolites are from Li et al. (2009); Himalayan leucogranites (GP-05, GP-09 and DZ-15) are from Guo and Wilson (2012); Triassic to Jurassic basalts from southern Lhasa are from Kang et al. (2014), Wei et al. (2017), Wang et al. (2016), and Zhu et al. (2008); late Carboniferous to Permian basalts from central Lhasa are from Geng et al. (2009) and Zhu et al. (2010); Triassic to Cretaceous Gangdese granites are from Chu et al. (2006), Wang et al. (2016), Wei et al. (2017), Wen et al. (2008), and Zhu et al. (2008); global subducting sediment are from Plank and Langmuir (1998). The bivariate mixture calculations use mixing equation of Faure (1986) and indicate a metasomatized mantle by sediment melts/fluids and a hybrid source consist of metasedimentary and minor (5–10%) basaltic melt. Symbols are as in Figure 6.

(with an average of 2.8 ppm), which also plot between MORB (0.12 ppm) and average global subducting sediment (= 6.9 ppm) or upper crust (10.5 ppm). These can plausibly be attributed to involvement of sediments or crustal materials at a convergent margin (Plank, 2005; Rudnick & Gao, 2014).

During the Late Paleozoic, the Lhasa Block has been proposed to be either a passive margin of the Gondwana supercontinent (Garzanti et al., 1999; Golonka & Ford, 2000) or a back-arc area related to southward subduction of the Proto- or Paleo-Tethyan Ocean (Cawood, et al., 2007; Dong et al., 2014; Guo et al., 2016; Zhu et al., 2013). Rift basalts formed in passive continental extension setting usually have alkaline or peralkaline affinities (Garland et al., 1995; Pin & Paquette, 1997; Wilson, 1989) or high Ti/Y ratios (>400; Pearce, 1982; Zhu et al., 2010), which is not consistent with the subduction-related geochemical features of the Zhengga mafic rocks. On the other hand, back-arc basin basalts are commonly formed by the upwelling asthenosphere in a suprasubduction zone setting and the vast majority have geochemical signatures of both MORB and arc volcanic rocks (e.g., Gribble et al., 1996, 1998; Schellart et al., 2006). Such features are generally acknowledged to be unique to back-arc basin basalts (e.g., Gribble et al., 1996, 1998). The Zhengga mafic rocks display distinct depletions in HFSE (e.g., $(Nb/La)_{PM}$ = 0.18–0.49; Figure 6c), which can be attributed to the immobility of HFSE in fluids derived from the subducting oceanic crust and/or sediments at a convergent margin (e.g., Elliott, 2003; Hastie et al., 2009). High $\varepsilon_{Nd}(t)$ values (up to +8.0; Table 2) are similar to those of the Paleo-Tethyan ophiolites (Li et al., 2009; Figure 7). In addition, the Zhengga mafic rocks collectively exhibit a range of other compositional features (e.g., Ti/V = 20–33; La/Nb = 2–8) that support formation in a back–arc basin setting (Figure 8). On the Th/Yb versus Ta/Yb diagrams (Figure S3), the Zhengga mafic rocks all plot within field of the continental arc basalt rather than the oceanic arc basalt, suggesting an intracontinental back-arc setting.

In conclusion, the latest Devonian Zhengga mafic rocks, located in southern Lhasa, were likely derived by decompression melting of asthenosphere metasomatised by subducted sediment and crustal materials in an intracontinental back-arc extension setting.

5.2. Petrogenesis of Zhengga Felsic Rocks

The Zhengga felsic rocks are characterized by markedly high and variable SiO_2, Al_2O_3, and low MgO contents with high A/CNK and negative $\varepsilon_{Nd}(t)$ values (−8.6 to −7.8; Figures 7 and S4). The major element compositional gap and distinct Nd-Hf-O isotope signatures between the Zhengga felsic and mafic rocks suggest that the felsic magmas are unlikely to have resulted from fractional crystallization of associated basaltic magmas accompanied by crustal contamination (Figures 5 and 7). This is confirmed by AFC modeling, which shows that a crustal input of 90% to the Zhengga mafic magmas would be needed to replicate the composition of the felsic magmas (Figure 7).

Although the high and variable A/CNK ratios of the Zhengga felsic rocks may result from their K_2O contents being affected by alteration, their high SiO_2 and Al_2O_3 contents and negative $\varepsilon_{Nd}(t)$ values in addition to the presence of aluminous minerals (muscovite and garnet) all imply that they are derived from a crustal source (Figures 4 and 7). Furthermore, their low Nb/U (1.7–7.2) ratios are similar to upper continental crust (4.4–

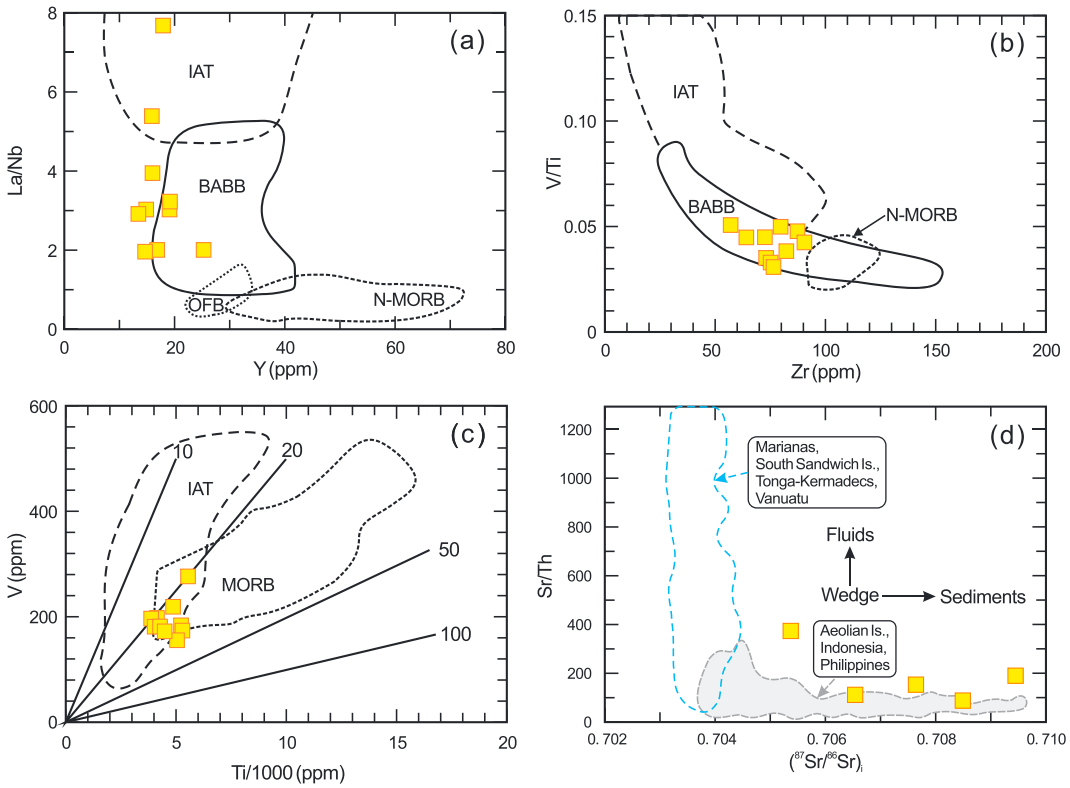

Figure 8. (a) La/Nb versus Y (Floyd, 1993), (b) V/Ti versus Zr (Woodhead et al., 1993), (c) V versus Ti/1000, and (d) Sr/Th versus $(^{87}Sr/^{86}Sr)_i$ tectonic and composition diagrams for Zhengga mafic rocks. BABB = back-arc basin basalt; N-MORB = normal mid-ocean ridge basalt.

8.9; Rudnick & Gao, 2014; Taylor & McLennan, 1985). The negative $\varepsilon_{Nd}(t)$ values and ancient Nd model ages (2.10 to 1.83 Ga) of the Zhengga felsic samples are also similar to those of the metasediment-derived Himalayan leucogranites (e.g., Guo & Wilson, 2012), which further supports an upper crustal source.

Zircon $\delta^{18}O$ values (7.3–10.8‰) of the Zhengga felsic rocks (Table S2) are equivalent to bulk-rock values of 9.9–13.4‰ and are consistent with supracrustal clastic sediment components (>10‰; Valley et al., 2005). Despite this, these values are slightly lower than zircon $\delta^{18}O$ values (8–12‰) of Great Himalayan pure sediment-derived granites (Hopkinson et al., 2017), suggesting that a low $\delta^{18}O$ component also contributed to the generation of the Zhengga felsic rocks. This, combined with their somewhat elevated Cr (up to 110 ppm) contents and higher $\varepsilon_{Nd}(t)$ values (−8.6 to −6.7) compared to the metasedimentary-derived leucogranites from the central Lhasa ($\varepsilon_{Nd}(t)$: −13.7 to −10.6; Liu et al., 2006) and Himalaya areas (−17.5 to −10.5; Guo & Wilson, 2012) also supports a potential input of a small amount of mantle-derived magma to the Zhengga felsic magmas.

Calculation of zircon saturation temperatures (T_{Zr}) using the updated equation proposed by Boehnke et al. (2013) and monazite saturation temperatures (T_{LREE}) after Montel (1993) yield 689 to 764 °C and 655 to 760 °C, respectively (Table 1). Within the uncertainties of less than 10%, T_{Zr} and T_{LREE} are broadly similar and suggest temperatures of formation within the range of 700–760 °C for the Zhengga felsic rocks. Underplating of the coeval mantle-derived magma could provide the heat source for melting of the middle and upper crust. Furthermore, garnet usually is a residual mineral for crustal melting; however, in the case of the Zhengga felsic rocks, with high Y (23–65 ppm and Table 1) and relatively flat HREE patterns (Figure 6c), garnet seems unlikely to be a major residual mineral, which may imply a low pressure (<7 kbar) of melting (Patiño Douce & Beard, 1996).

The Zhengga felsic rocks display variable SiO_2 (65.4–77.3 wt.%) and Al_2O_3 (11.5–17.3 wt.%) contents with negative Eu anomalies (Eu/Eu* ratios from 0.25 to 0.87; Figure 6c), indicating plagioclase and/or K-

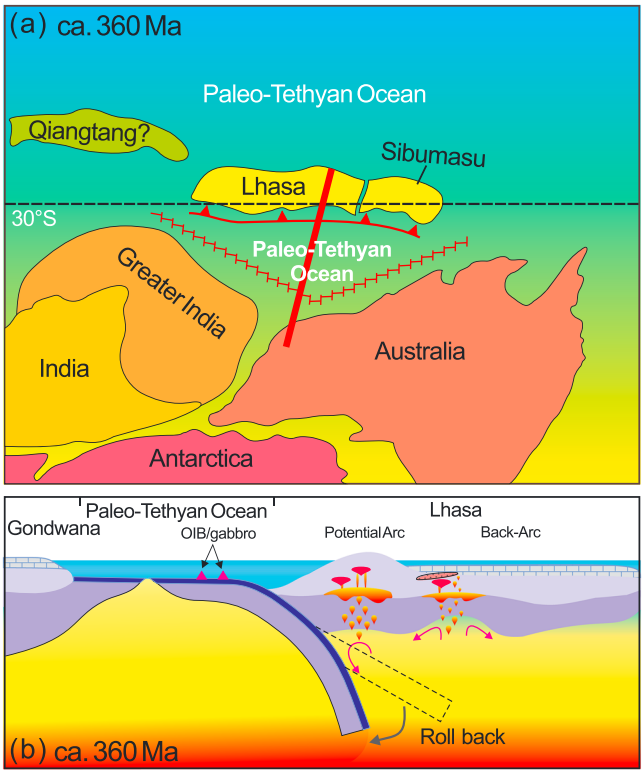

Figure 9. (a) Top view and (b) section view schematic illustrations of the nature and evolution of the Tibetan Plateau from the latest Devonian.

feldspar fractionation. Fractionation of plagioclase would result in negative Sr-Eu anomalies, and that of K-feldspar would produce negative Eu-Ba anomalies (Wu et al., 2003). The good negative correlation between Al_2O_3 and Ba contents with increasing SiO_2 contents (Figure S5) suggests that the Zhengga felsic rocks more likely experienced various degrees of K-feldspar fractionation.

To conclude, we consider that the latest Devonian Zhengga felsic rocks were generated from melting of metasedimentary rocks at 700–760 °C. These melts subsequently underwent recharge with a small amount of mafic magma and fractional crystallization of K-feldspar in mid-upper crust (~10–20 km) magma chambers.

5.3. Late Paleozoic Magmatism and Tectonic Evolution of Lhasa Block

Compared to other blocks that rifted from the Gondwana supercontinent, such as Yangtze, North China, Tarim, Indochina/East Malaya/West Sumatra, Sibumasu, and West Burma (e.g., Cawood, et al., 2007; Metcalfe, 2006, 2013; Torsvik et al., 2012), relatively little is known about the Late Paleozoic tectonic evolution of the Lhasa Block. The Late Devonian to Early Carboniferous magmatism reported in this study sheds new light on the evolution of the Lhasa Block and the tectonic reconstruction of Gondwana.

Late Devonian to Early Carboniferous magmatism in the Lhasa Block is mainly found in the eastern segment (~200 km between Sangri and Nang; Dong et al., 2010, 2014; Ji et al., 2012; this study) and in the Zhongba and Xiongcun areas of the western segment (Dai et al., 2011; Lang et al., 2017) of the southern Lhasa subblock (Figure 2 and Table S4). The Zhongba and Xiongcun gabbros were emplaced at 342 and 363 Ma, respectively, and both were suggested as remnants of Paleo-Tethyan oceanic crust (Dai et al., 2011; Lang et al., 2017). In contrast, the magmatic rocks from Sangri to Nang are mainly granitoids and associated amphibolites, and they represent a bimodal igneous association formed in a back-arc extensional setting (Dong et al., 2014; Ji et al., 2012; Zhu et al., 2013 and this study). The granitoids were primarily intruded between 371 and 345 Ma, while the mafic rocks were generally emplaced from 365 to 353 Ma (Dong et al., 2010, 2014; Ji et al., 2012; this study; Table S4).

Previous studies mainly favor a back-arc spreading setting for the northern margin of Gondwana related to southward subduction of Proto- or Paleo-Tethyan Ocean that is represented by Bangong-Nujiang suture and Longmu Tso-Shuanghu Suture Zone during the Paleozoic (Cawood, et al., 2007; Dong et al., 2014; Guo et al., 2016; Zhu et al., 2010, 2013). In this tectonic scenario, the Lhasa Block did not rift away from the northern margin of Gondwana until the Early Permian (e.g., Enkin et al., 1992; Zhu et al., 2010, 2013) or even later (Late Permian to Late Triassic; e.g., Dong et al., 2014; Ferrari et al., 2008; Golonka & Ford, 2000; Metcalfe, 2006, 2013). As discussed above, however, the Zhengga mafic rocks show affinities of intracontinental back-arc basalt, suggesting a subduction-related, rather than passive continent margin, setting. In addition, the expected Late Paleozoic arc-type magmatism is not found in northern and central Lhasa subblocks, where the Devonian to Early Carboniferous limestone was deposited (Figure S1), which is also inconsistent with a southward subduction scenario.

Instead, we suggest that the Lhasa Block may have been a microcontinent isolated in the Paleo-Tethyan Ocean basin, during the Late Devonian to Early Carboniferous time (Figure 9a). In this conceptual model, the latest Devonian bimodal magmatism in southern Lhasa was caused by northward subduction of the branch Paleo-Tethyan Ocean (Figure 9b). Our model is based on the following evidence: (1) Late Devonian (364 Ma) OIB-type alkaline amphibolites have been found in the mélange zone of the western Indus-Yarlung Tsangpo suture to the south of Lhasa Block (Figure 1; Dai et al., 2011). This is not an isolated case and the Early Carboniferous (341 Ma) gabbros found in Xigaze area also are considered as a

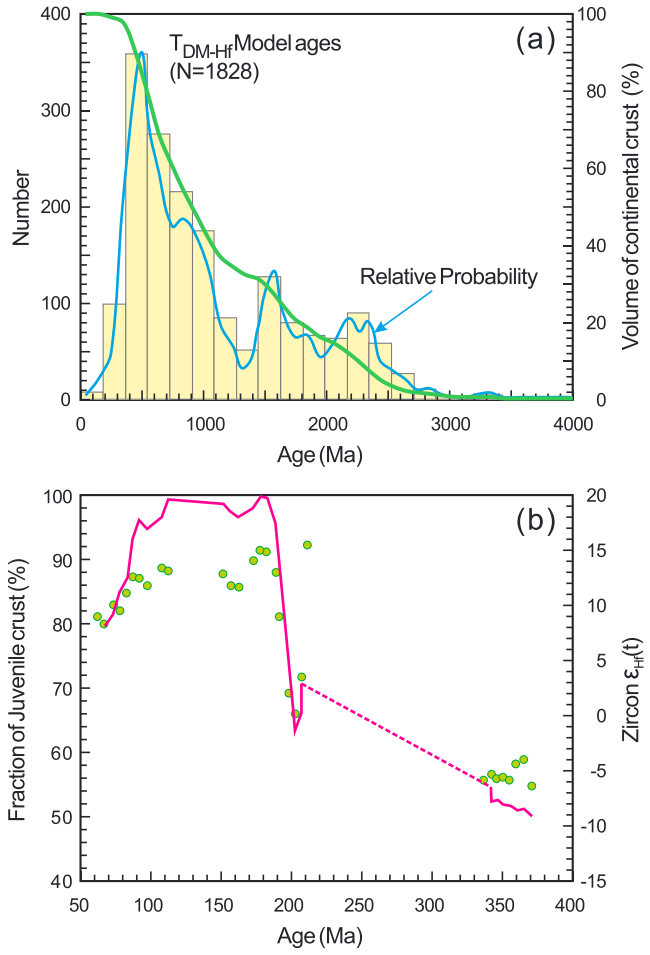

Figure 10. (a) Histogram of zircon Hf model age for magmatic rocks in the southern Lhasa. The green line indicates the crustal growth model. (b) Juvenile input for southern Lhasa calculated from the zircon Hf isotope data shown by red broken line (details see text), compared with the average $\varepsilon_{Hf}(t)$ values for granitic rocks shown by green cycles (Table S5). All calculations are presented for 5 Ma time intervals. Southern Lhasa could experience significant episodic crustal growth and reworking during Late Paleozoic to Mesozoic.

remnant of Paleo-Tethyan Oceanic crust (Lang et al., 2017). Likewise, ^{39}Ar-^{40}Ar dating of clinopyroxene and plagioclase from the layered amphibolites identified in the Luobusha ophiolite of the east Indus-Yarlung Tsangpo suture yield an Early Carboniferous age of 353–352 Ma (Mo et al., 2008; Figure 3). All these indicate the existence of potential Paleo-Tethyan oceanic crust separating the Lhasa block from the Gondwana continent during the Late Devonian to Early Carboniferous (Figure 9), which is similar to the Sibumasu (Jian et al., 2009; Wang et al., 2012). (2) As mentioned above, an arc-related affinity of the Zhengga mafic rocks and widespread coeval bimodal magmatism in the southern Lhasa is inconsistent with a passive rift or extension in Lhasa as part of northern margin of the Gondwana (Garzanti et al., 1999; Golonka & Ford, 2000). In addition, on the another scenario that the Paleo-Tethyan Ocean slab southward subducted beneath northern Gondwana (Guo et al., 2016; Zhu et al., 2013), given the back-arc magmatism in the southern (Dong et al., 2014; Ji et al., 2012; this study), a magmatic arc would be expected to be found in north central Lhasa. However, widespread Devonian to Carboniferous carbonate but lack of arc-type magmatism in central and northern Lhasa, are inconsistent with a southward subduction model. Thus, a model invoking northward subduction of the Paleo-Tethyan slab is more consistent with the occurrence of late Paleozoic shallow marine carbonate platform sedimentary rocks in central Lhasa and coeval back-arc bimodal magmatism in the southern Lhasa (Figure 9b). It is also worth noting that northward drift of all of the continental fragments that rifted from Gondwana is also supported by the evidence for general northward convective mantle circulation during Late Paleozoic-Mesozoic evolution of Tethys (Sengor, 1987; Stampfli et al., 2013).

We therefore suggest that a potential Late Devonian-Carboniferous continental arc might have existed farther south of present-day southern Lhasa (Figure 9b), given significant subduction erosion and crustal reworking during the Mesozoic to Cenozoic (Hu et al., 2014). Future detailed work on identification of Late Paleozoic ophiolites in the Indus-Yarlung Tsangpo, Bangong-Nujiang, and Longmu Tso-Shuanghu Suture Zones as well as coeval arc magmatism in Lhasa will provide a test for the tectonomagmatic models proposed by this and previous studies (e.g., Dan et al., 2018; Dong et al., 2014; Guo et al., 2016; Ji et al., 2012; Zhu et al., 2013).

5.4. Nature and Evolution of Continental Crust in Southern Lhasa

It is generally accepted that significant Phanerozoic crustal growth occurred in southern Lhasa (e.g., Hou et al., 2015; Ji et al., 2009; Niu et al., 2013; Zhu et al., 2011). Broadly speaking two models have been proposed to account for the timing and mechanism of crustal growth in the region. The first proposes that the underplating of mantle-derived mafic magmas and the recycling of subducted oceanic crust during Neo-Tethyan subduction played an important role in crustal growth (e.g., Hou et al., 2015; Ji et al., 2009; Ma et al., 2013; Wei et al., 2017). The second model argues that continental collision zones were the primary sites of net continental crust growth (e.g., Mo et al., 2007; Niu et al., 2013; Zhu et al., 2013). However, both models mainly focus on localized apparent age and the pre-Mesozoic crustal evolution history of southern Lhasa remains poorly understood. We have therefore compiled almost 3000 zircon Hf isotope and 248 whole-rock Nd isotope analyses from magmatic rocks of southern Lhasa in order to assess crustal evolution of the block through time.

Granitic rocks dominate the preserved magmatic record in southern Lhasa, and thus, discussion of new continental crust formation has focused on the granitic rocks in this study. The Hf model age of granitoids indicate that ~90% of crust in southern Lhasa was formed during 2500 to 550 Ma at a gradually increasing growth

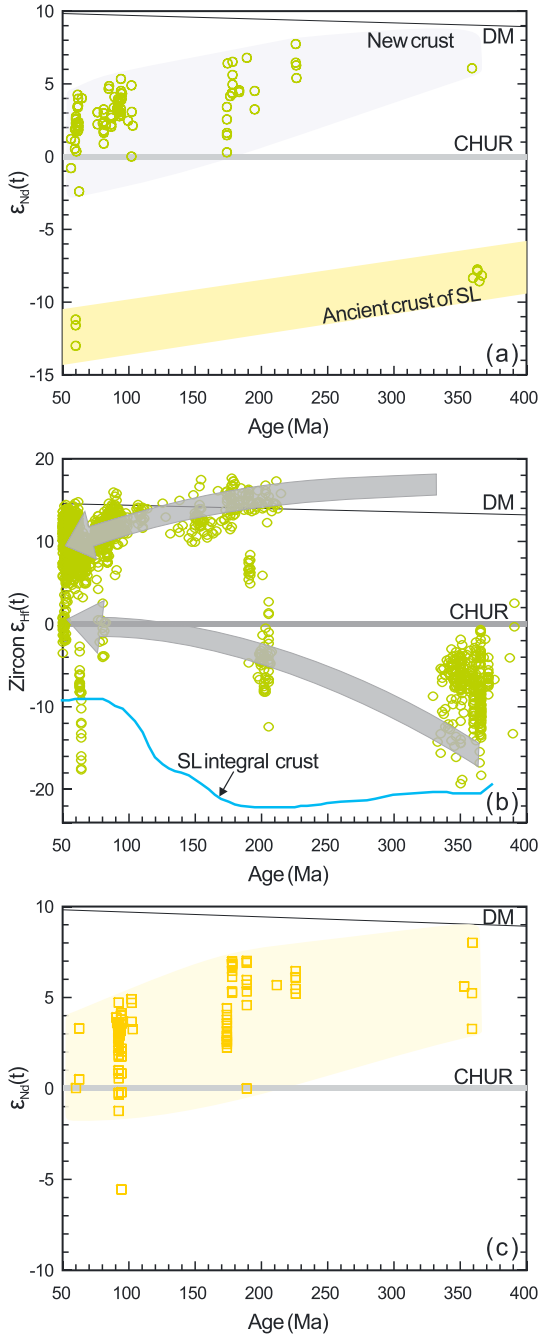

Figure 11. (a, b) Whole rock Nd and zircon Hf isotopic values of granitic rocks (SiO_2 > 56 wt.%) from the southern Lhasa; (c) whole rock $\varepsilon_{Nd}(t)$ isotopic ratios of mafic rocks (SiO_2 < 53 wt.%) plotted as a function of crystallization ages. The global depleted mantle value was used as the juvenile endmember, with $^{176}Hf/^{177}Hf$ at the present day of 0.28325 (Griffin et al., 2000). Integral crust curves in (b) represent the Hf composition of the local crust basement calculated using the method described in Belousova et al. (2010). These curves represent the average Hf isotope composition of the local continental crust at time t, estimated from all the detrital zircons that crystallized before time *t* (Table S5), using the average $^{176}Lu/^{177}Hf$ of the continental crust (0.0125; Belousova et al., 2010). DM = depleted mantle; CHUR = chondritic uniform reservoir.

rate (Figure 10a). Thus, the significant period of crustal generation in southern Lhasa appears to have occurred substantially earlier than previously thought (i.e., the Late Triassic to Early Tertiary; e.g., Ji et al., 2009; Ma et al., 2013; Niu et al., 2013; Wei et al., 2017; Zhu et al., 2013).

The wide range of radiogenic Nd-Hf isotope compositions for the Phanerozoic granitic rocks require at least two distinct crustal components to be involved in the genesis of these magmas in southern Lhasa (Figure 11). One with high Nd-Hf isotopic ratios likely represents juvenile crust, whereas another with low $\varepsilon_{Nd}(t)$ and zircon $\varepsilon_{Hf}(t)$ values (down to −9 and −13, respectively) is likely to be reworked ancient crust (Figures 11a and 11b). In this study, the distinct Nd-Hf-O isotopic composition of Devonian-Carboniferous mafic and felsic rocks also support presence of two crustal end-members beneath the southern Lhasa during the Late Paleozoic (Figure 7).

The contracting wedge-shaped array such that zircon $\varepsilon_{Hf}(t)$ values becomes increasingly juvenile and less diverse during Late Devonian to Eocene (Figure 11b) indicates the ancient crust in southern Lhasa was likely replaced by juvenile crust over time. Two component mixing calculations can estimate the contribution of two components over time (Figure 10b). On this diagram, the crustal end-member is represented by the integral crust (Figure 11b), and the juvenile component is characterized by the mafic rocks that are coeval with the granitic rocks (Table S5).

Although this figure represents an approximation, it does give an overview of the crustal evolution from the Devonian to the Tertiary and suggests that southern Lhasa experienced variable crustal growth and reworking (Figure 10). Our data imply that the latest Devonian (ca. 360 Ma) granitoid magmatism contains ~60% juvenile component (Figure 10b). In combination with widespread coeval mafic rocks (Figure. 2; Dong et al., 2014; Ji et al., 2012), the Zhengga mafic rocks with high $\varepsilon_{Nd}(t)$ and $\varepsilon_{Hf}(t)$ values support significant crustal growth in southern Lhasa during Devonian-Carboniferous (Figure 7). Thus, our results indicate that the Paleozoic is a likely period of juvenile crustal accretion in the southern Lhasa Block, and the crustal growth is likely greater than reworking at this time. The magmatic record during this time is still poorly constrained and more studies on Pre-Mesozoic magmatism in Lhasa will be critical and able to verify or refine this model.

As indicated by previous research (e.g., Ji et al., 2009; Ma et al., 2013; Wei et al., 2017), the Early Jurassic to early Late Cretaceous (ca. 200–90 Ma) appears to represent one of the most significant periods of crustal growth in southern Lhasa. Meaningfully, the significant increase in juvenile input (~30 percentage points; Figure 10b), accompanied by the abrupt shift of integral crust curve (Figure 11b), indicate intense crustal growth in a short interval (200–180 Ma). After that, the addition of new material by arc magmatism appears to be balanced by the return of crust into the mantle until the Late Cretaceous. A decrease in mantle input since then can be observed (Figure 10b), suggesting raising crustal reworking during 90 to 60 Ma.

The more restricted range in zircon ε_{Hf} reflects diminishing crustal reworking and increasing mantle input over time, which is suggested to represent a fingerprint of external orogens (Collins et al., 2011). Southern Lhasa during Late Paleozoic to Mesozoic was likely to have been such an external orogen, where the old crust is removed due to sediment

subduction and subduction erosion and replaced by newly formed crust. During evolution of external orogen, repetition of these processes along with crustal remelting, led to the range of radioactive Nd-Hf isotope signatures gradually narrowing and becoming juvenile until the removed component is similar to new material (Collins et al., 2011). Our study thus suggests that the southern Lhasa has experienced significant building and reworking of continental crust during Paleozoic to Mesozoic and was transformed from an ancient microcontinent into a new terrane. The rate of continental crust generation relative to crust destruction likely have been greater at certain times, such as the latest Devonian and Early Jurassic (Figure 10b).

The external and internal orogenic systems are proposed as two fundamental dynamic evolution of Earth (Collins et al., 2011). Crustal growth is generally greater than reworking in the external orogen, whereas crustal reworking is stronger in the internal orogen. However, these two systems may alternate in the same orogenic belt, even repeatedly. Such information may be particularly helpful in young orogens where the ancient lithological record is only very incompletely preserved, largely hidden below younger rocks, or tectonically dismembered. Thus, the study of crustal growth for the young orogens needs to fully consider and evaluate the influence of crustal reworking.

6. Conclusions

1. Bimodal magmatic rocks comprising amphibolites and two-mica gneissic granites in Zhengga area, southern Tibet, were emplaced in the latest Devonian to earliest Carboniferous (ca. 366–353 Ma).
2. The Zhengga mafic rocks were generated by decompression melting of metasomatized asthenosphere associated with intracontinental back-arc extension.
3. The Zhengga two-mica gneissic granites were derived from an ancient metasedimentary source and subsequently underwent minor mafic magma recharge and fractional crystallization of K-feldspar.
4. The southern Lhasa Block was once a microcontinent with Precambrian basement and transformed into juvenile terrane by significant Phanerozoic crustal growth and reworking.

Acknowledgments
Presented data are available by request from the corresponding author. We thank Kuo-Lung Wang and two other anonymous reviewers for constructive reviews and comments that have greatly improved the quality of this paper; and Editor Stephen Parman and Associate Editor Fang-Zhen Teng for comments and editorial handling. We appreciate the assistance of Yue-Heng Yang, Xi-Rong Liang, Xiang-Lin Tu, Jin-Long Ma, Sheng-Ling Sun, Qing Yang, Wan-Feng Zhang, Bo-Qin Xiong, Guang Qian Hu, and Ying Liu for zircon age, whole rock, and mineral geochemical analyses. Financial support for this research was provided by the National Key Research and Development Project (2016YFC0600309), the Strategic Priority Research Program (A) of the Chinese Academy of Sciences (XDA2007030402), the National Natural Science Foundation of China (41872062, 91855215, and 41630208), the Second Tibetan Plateau Scientific Expedition and Research (STEP; 2019QZKK0702), the Key Program of the Chinese Academy of Sciences (QYZDJ-SSW-DQC026), the Key Program of Guangzhou City (201707020032), Youth Innovation Promotion Association CAS (2017404), and the Guangzhou Institute of Geochemistry, Chinese Academy of Sciences (GIGCAS 135 project 135TP201601). This is contribution IS-XXXX from GIGCAS. The data supporting these conclusions can be found in EarthChem Library (DOI: 10.1594/IEDA/111292, http://www.earthchem.org/library) and supporting information Figures S1–S5 and Tables S1–S5.

References

Aitchison, J. C., Davis, A. M., Abrajevitch, A. V., Ali, J. R., Liu, J., Luo, H., et al. (2003). Stratigraphic and sedimentological constraints on the age and tectonic evolution of the Neotethyan ophiolites along the Yarlung Tsangpo suture zone, Tibet. *Geological Society, London, Special Publications*, *218*(1), 147–164. https://doi.org/10.1144/GSL.SP.2003.218.01.09

Amelin, Y., Lee, D. C., Halliday, A. N., & Pidgeon, R. T. (1999). Nature of the Earth's earliest crust from hafnium isotopes in singledetrital zircons. *Nature*, *399*, 1497–1503.

Belousova, E. A., Kostitsyn, Y. A., Griffin, W. L., Begg, G. C., O'Reilly, S. Y., & Pearson, N. J. (2010). The growth of the continental crust: Constraints from zircon Hf-isotope data. *Lithos*, *119*(3-4), 457–466. https://doi.org/10.1016/j.lithos.2010.07.024

Boehnke, P., Watson, E. B., Trail, D., Harrison, T. M., & Schmitt, A. K. (2013). Zircon saturation re-revisited. *Chemical Geology*, *351*, 324–334. https://doi.org/10.1016/j.chemgeo.2013.05.028

Castillo, P. R., Janney, P. E., & Solidum, R. U. (1999). Petrology and geochemistry of Camiguin Island, southern Philippines: Insights to the source of adakites and other lavas in a complex arc setting. *Contributions to Mineralogy and Petrology*, *134*(1), 33–51. https://doi.org/10.1007/s004100050467

Cawood, P. A., Johnson, M. R. W., & Nemchin, A. A. (2007). Early Palaeozoic orogenesis alongthe Indian margin of Gondwana: tectonic response to Gondwana assembly. *Earth and Planetary Science Letters*, *255*, 70–84.

Chu, M. F., Chung, S. L., Song, B., Liu, D., O'Reilly, S. Y., Pearson, N. J., et al. (2006). Zircon U-Pb and Hf isotope constraints on the Mesozoic tectonics and crustal evolution of southern Tibet. *Geology*, *34*(9), 745–748. https://doi.org/10.1130/G22725.1

Chung, S. L., Chu, M. F., Zhang, Y., Xie, Y., Lo, C. H., Lee, T. Y., et al. (2005). Tibetan tectonic evolution inferred from spatial and temporal variations in post–collisional magmatism. *Earth–Science Reviews*, *68*(3–4), 173–196.

Collins, W. J., Belousova, E. A., Kemp, A. I. S., & Murphy, J. B. (2011). Two contrasting Phanerozoic orogenic systems revealed by hafnium isotope data. *Nature Geoscience*, *4*(5), 333–337. https://doi.org/10.1038/ngeo1127

Dai, J., Wang, C., Hébert, R., Li, Y., Zhong, H., Guillaume, R., et al. (2011). Late Devonian OIB alkaline gabbro in the Yarlung Zangbo suture zone: Remnants of the Paleo-Tethys? *Gondwana Research*, *19*(1), 232–243. https://doi.org/10.1016/j.gr.2010.05.015

Dan, W., Wang, Q., Zhang, X.-Z., Zhang, C., Tang, G.-J., Wang, J., et al. (2018). Magmatic record of Late Devonian arc-continent collision in the northern Qiangtang, Tibet: Implications for the early evolution of East Paleo-Tethys Ocean. *Lithos*, *308-309*, 104–117. https://doi.org/10.1016/j.lithos.2018.03.002

DePaolo, D. J. (1998). Neodymium Isotope Geochemistry. An Introduction (pp 187). New York: Springer-Verlag. https://doi.org/10.1007/978-3-642-48916-7

Dhuime, B., Hawkesworth, C. J., Cawood, P. A., & Storey, C. D. (2012). A Change in the Geodynamics of Continental Growth 3 Billion Years Ago. *Science*, *335*(6074), 1334–1336. https://doi.org/10.1126/science.1216066

Dong, X., Zhang, Z., Liu, F., He, Z., & Lin, Y. (2014). Late Paleozoic intrusive rocks from the southeastern Lhasa terrane, Tibetan Plateau, and their Late Mesozoic metamorphism and tectonic implications. *Lithos*, *198*, 249–262.

Dong, X., Zhang, Z., Liu, F., Wang, W., Yu, F., & Shen, K. (2011). Zircon U–Pb geochronology of the Nyainqêntanglha Group from the Lhasa terrane: New constraints on the Triassic orogeny of the south Tibet. *Journal of Asian Earth Sciences*, *42*, 732–739.

Dong, X., Zhang, Z., & Santosh, M. (2010). Zircon U-Pb Chronology of the Nyingtri Group, Southern Lhasa Terrane, Tibetan Plateau: Implications for Grenvillian and Pan-African Provenance and Mesozoic-Cenozoic Metamorphism. *The Journal of Geology*, *118*(6), 677–690. https://doi.org/10.1086/656355

Elliott, T. (2003). Tracers of the slab. Inside the subduction Factory. *Geophysical Monograph Series*, *138*, 23–45.

Enkin, R. J., Yang, Z., Chen, Y., & Courtillot, V. (1992). Paleomagnetic constraints on the geodynamic history of the major blocks of China from the Permian to the present. *Journal of Geophysical Research*, *97*(B10), 13,953–13,989. https://doi.org/10.1029/92JB00648

Faure, G. (1986). *Principles of Isotope Geology* (pp. 608). Wiley.

Ferrari, O., Hochard, C., & Stampfli, G. (2008). An alternative plate tectonic model for the Palaeozoic–Early Mesozoic Palaeotethyan evolution of southeast Asia (Northern Thailand–Burma). *Tectonophysics*, *451*(1-4), 346–365. https://doi.org/10.1016/j.tecto.2007.11.065

Floyd, P. (1993). Geochemical discrimination and petrogenesis of alkalic basalt sequences in part of the Ankara melange, central Turkey. *Journal of the Geological Society*, *150*(3), 541–550. https://doi.org/10.1144/gsjgs.150.3.0541

Garland, F., Hawkesworth, C., & Mantovani, M. (1995). Description and Petrogenesis of the Paraná Rzhyolites, Southern Brazil. *Journal of Petrology*, *36*(5), 1193–1227. https://doi.org/10.1093/petrology/36.5.1193

Garzanti, E., Le Fort, P., & Sciunnach, D. (1999). First report of Lower Permian basalts in South Tibet: Tholeiitic magmatism during break-up and incipient opening of Neotethys. *Journal of Asian Earth Sciences*, *17*(4), 533–546. https://doi.org/10.1016/S1367-9120(99)00008-5

Geng, Q. R., Sun, Z. M., Pan, G. T., Zhu, D. C., & Wang, L. Q. (2009). Origin of the Gangdise (Transhimalaya) Permian arc in southern Tibet: Stratigraphic and volcanic geochemical constraints. *Island Arc*, *18*(3), 467–487. https://doi.org/10.1111/j.1440-1738.2009.00664.x

Golonka, J., & Ford, D. (2000). Pangean (late Carboniferous–Middle Jurassic) paleoenvironment and lithofacies. *Palaeogeography, Palaeoclimatology, Palaeoecology*, *161*(1-2), 1–34. https://doi.org/10.1016/S0031-0182(00)00115-2

Gribble, R. F., Stern, R. J., Bloomer, S. H., Stüben, D., O'Hearn, T., & Newman, S. (1996). MORB mantle and subduction components interact to generate basalts in the southern Mariana Trough back-arc basin. *Geochimica et Cosmochimica Acta*, *60*(12), 2153–2166. https://doi.org/10.1016/0016-7037(96)00078-6

Gribble, R. F., Stern, R. J., Newman, S., Bloomer, S. H., & O'Hearn, T. (1998). Chemical and isotopic composition of lavas from the northern Mariana Trough: Implications for magmagenesis in back-arc basins. *Journal of Petrology*, *39*(1), 125–154. https://doi.org/10.1093/petroj/39.1.125

Griffin, W. L., Pearson, N. J., Belousova, E., Jackson, S. E., Achterbergh, E.v., O'Reilly, S. Y., & Shee, S. R. (2000). The Hf isotope composition of cratonic mantle: LAM-MC-ICPMS analysis of zircon megacrysts in kimberlites. *Geochimica et Cosmochimica Acta*, *64*(1), 133–147. https://doi.org/10.1016/S0016-7037(99)00343-9

Guo, L., Zhang, H. F., Harris, N., Xu, W. C., & Pan, F. B. (2016). Late Devonian-Early Carboniferous magmatism in the Lhasa terrane and its tectonic implications: Evidences from detrital zircons in the Nyingchi Complex. *Lithos*, *245*, 47–59. https://doi.org/10.1016/j.lithos.2015.06.018

Guo, Z., & Wilson, M. (2012). The Himalayan leucogranites: Constraints on the nature of their crustal source region and geodynamic setting. *Gondwana Research*, *22*(2), 360–376. https://doi.org/10.1016/j.gr.2011.07.027

Guynn, J. H., Kapp, P., Pullen, A., Heizler, M., Gehrels, G., & Ding, L. (2006). Tibetan basement rocks near Amdo reveal "missing" Mesozoic tectonism along the Bangong suture, central Tibet. *Geology*, *34*(6), 505–508. https://doi.org/10.1130/G22453.1

Hastie, A. R., Kerr, A. C., Mitchell, S. F., & Millar, I. L. (2009). Geochemistry and tectonomagmatic significance of Lower Cretaceous island arc lavas from the Devils Racecourse Formation, eastern Jamaica. *Geological Society, London, Special Publications*, *328*(1), 339–360. https://doi.org/10.1144/SP328.14

Hastie, A. R., Kerr, A. C., Pearce, J. A., & Mitchell, S. F. (2007). Classification of altered volcanic island arc rocks using immobile trace elements: Development of the Th Co discrimination diagram. *Journal of Petrology*, *48*(12), 2341–2357. https://doi.org/10.1093/petrology/egm062

Hastie, A. R., Mitchell, S. F., Treloar, P. J., Kerr, A. C., Neill, I., & Barfod, D. N. (2013). Geochemical components in a Cretaceous island arc: The Th/La–(Ce/Ce*)Nd diagram and implications for subduction initiation in the inter-American region. *Lithos*, *162-163*, 57–69. https://doi.org/10.1016/j.lithos.2012.12.001

Hawkesworth, C. J. & Kemp, A. I. S. (2006). Evolution of the continental crust. *Nature*, *443*, 811–817. https://doi.org/10.1038/nature05191

Hofmann, A. (1997). Mantle geochemistry: The message from oceanic volcanism. *Nature*, *385*(6613), 219–229. https://doi.org/10.1038/385219a0

Hopkinson, T. N., Harris, N. B. W., Warren, C. J., Spencer, C. J., Roberts, N. M. W., Horstwood, M. S. A., Parrish, R. R., & Eimf (2017). The identification and significance of pure sediment-derived granites. *Earth and Planetary Science Letters*, *467*, 57–63. https://doi.org/10.1016/j.epsl.2017.03.018

Hoskin, P., & Black, L. (2000). Metamorphic zircon formation by solid state recrystallization of protolith igneous zircon. *Journal of Metamorphic Geology*, *18*, 423–439.

Hou, Z., Yang, Z., Lu, Y., Kemp, A., Zheng, Y., Li, Q., et al. (2015). A genetic linkage between subduction- and collision-related porphyry Cu deposits in continental collision zones. *Geology*, *43*, 643–650.

Hu, X. M., An, W., Wang, J. G., Garzanti, E., & Guo, R. H. (2014). Himalayan detrital chromian spinels and timing of Indus-Yarlung ophiolite erosion. *Tectonophysics*, *621*, 60–628.

Jagoutz, O. E., Burg, J.-P., Hussain, S., Dawood, H., Pettke, T., Iizuka, T., & Maruyama, S. (2009). Construction of the granitoid crust of an island arc. Part I: Geochronological and geochemical constraints from the plutonic Kohistan (NW Pakistan). *Contributions to Mineralogy and Petrology*, *158*(6), 739–755. https://doi.org/10.1007/s00410-009-0408-3

Ji, W. Q., Wu, F. Y., Chung, S. L., Li, J. X., & Liu, C. Z. (2009). Zircon U-Pb geochronology and Hf isotopic constraints on petrogenesis of the Gangdese batholith, southern Tibet. *Chemical Geology*, *262*(3-4), 229–245. https://doi.org/10.1016/j.chemgeo.2009.01.020

Ji, W. Q., Wu, F. Y., Liu, C. Z., & Chung, S. L. (2012). Identification of Early Carboniferous granitoids from Southern Tibet and implication for terrane assembly related to the Paleo-Tethyan evolution. *The Journal of Geology*, *120*(5), 531–541. https://doi.org/10.1086/666742

Jian, P., Liu, D., Kröner, A., Zhang, Q., Wang, Y., Sun, X., & Zhang, W. (2009). Devonian to Permian plate tectonic cycle of the Paleo-Tethys Orogen in southwest China (I): Geochemistry of ophiolites, arc/back-arc assemblages and within-plate igneous rocks. *Lithos*, *113*(3-4), 748–766. https://doi.org/10.1016/j.lithos.2009.04.004

Kang, Z.-Q., Xu, J.-F., Wilde, S. A., Feng, Z.-H., Chen, J.-L., Wang, B.-D., et al. (2014). Geochronology and geochemistry of the Sangri Group Volcanic Rocks, Southern Lhasa Terrane: Implications for the early subduction history of the Neo-Tethys and Gangdese Magmatic Arc. *Lithos*, *200*, 157–168.

Kapp, P., DeCelles, P. G., Gehrels, G. E., Heizler, M., & Ding, L. (2007). Geological records of the Lhasa-Qiangtang and Indo-Asian collisions in the Nima area of central Tibet. *Geological Society of America Bulletin*, *119*(7-8), 917–933. https://doi.org/10.1130/B26033.1

Kemp, A. I. S., & Hawkesworth, C. J. (2014). 4.11 - Growth and Differentiation of the Continental Crust from Isotope Studies of Accessory Minerals A2. *Treatise on Geochemistry*, *379-421*. https://doi.org/10.1016/B978-0-08-095975-7.00312-0

Kersting, A. B., & Arculus, R. J. (1994). Klyuchevskoy volcano, Kamchatka, Russia: The role of high-flux recharged, tapped, and fractionated magma chamber (s) in the genesis of high-Al2O3 from high-MgO basalt. *Journal of Petrology*, *35*(1), 1–41. https://doi.org/10.1093/petrology/35.1.1

Korenaga, J. (2018). Estimating the formation age distribution of continental crust by unmixing zircon ages. *Earth and Planetary Science Letters*, *482*, 388–395. https://doi.org/10.1016/j.epsl.2017.11.039

Lang, X. H., Tang, J. X., Deng, Y. L., Xie, F. W., Yang, Z. Y., Cui, Z. W., et al. (2017). The First Discovery of Early Carboniferous Gabbro in Xiongcun Area on the Southern Margin of Lhasa Terrane, Tibet: Remnants of Paleo-Tethys Ocean? *Acta Geoscientica Sinica*, *38*(5), 745–753.

Lee, H. Y., Chung, S. L., Lo, C. H., Ji, J., Lee, T. Y., Qian, Q., & Zhang, Q. (2009). Eocene Neotethyan slab breakoff in southern Tibet inferred from the Linzizong volcanic record. *Tectonophysics*, *477*(1-2), 20–35. https://doi.org/10.1016/j.tecto.2009.02.031

Leier, A. L., Kapp, P., Gehrels, G. E., & DeCelles, P. G. (2007). Detrital zircon geochronology of Carboniferous–Cretaceous strata in the Lhasa terrane, Southern Tibet. *Basin Research*, *19*(3), 361–378. https://doi.org/10.1111/j.1365-2117.2007.00330.x

Li, X., Tang, G., Gong, B., Yang, Y., Hou, K., Hu, Z., et al. (2013). Qinghu zircon: A working reference for microbeam analysis of U-Pb age and Hf and O isotopes. *Chinese Science Bulletin*, *58*(36), 4647–4654. https://doi.org/10.1007/s11434-013-5932-x

Li, X.-H., Li, W.-X., Li, Q.-L., Wang, X. C., Liu, Y., & Yang, Y.-H. (2010). Petrogenesis and tectonic significance of the ~850 Ma Gangbian alkaline complex in South China: Evidence from in Situ zircon U-Pb dating, Hf-O isotopes and whole-rock geochemistry. *Lithos*, *113*, 1–15.

Li, X. H., Liu, D., Sun, M., Li, W. X., Liang, X. R., & Liu, Y. (2004). Precise Sm-Nd and U-Pb isotopic dating of the supergiant Shizhuyuan polymetallic deposit and its host granite, SE China. *Geological Magazine*, *141*(2), 225–231. https://doi.org/10.1017/S0016756803008823

Li, X. H., Long, W. G., Li, Q. L., Liu, Y., Zheng, Y. F., Yang, Y. H., et al. (2010). Penglai zircon megacrysts: A potential new working reference material for microbeam determination of Hf–O isotopes and U–Pb age. *Geostandards and Geoanalytical Research*, *34*(2), 117–134. https://doi.org/10.1111/j.1751-908X.2010.00036.x

Li, X. H., Qi, C. S., Liu, Y., Liang, X. R., Tu, X. L., Xie, L. W., & Yang, Y. H. (2005). Petrogenesis of the Neoproterozoic bimodal volcanic rocks along the western margin of the Yangtze Block: New constraints from Hf isotopes and Fe/Mn ratios. *Chinese Science Bulletin*, *50*(21), 2481–2486. https://doi.org/10.1360/982005-287

Li, X. H., Zhou, H., Chung, S. L., Lo, C. H., Wei, G., Liu, Y., & Lee, C. Y. (2002). Geochemical and Sr-Nd isotopic characteristics of late Paleogene ultrapotassic magmatism in southeastern Tibet. *International Geology Review*, *44*(6), 559–574. https://doi.org/10.2747/0020-6814.44.6.559

Li, Z., Yang, J., Xu, Z., Li, T., Xu, X., Ren, Y., & Robinson, P. T. (2009). Geochemistry and Sm–Nd and Rb–Sr isotopic composition of eclogite in the Lhasa terrane, Tibet, and its geological significance. *Lithos*, *109*(3-4), 240–247. https://doi.org/10.1016/j.lithos.2009.01.004

Lin, Y.-H., Zhang, Z.-M., Dong, X., Shen, K., & Lu, X. (2013). Precambrian evolution of the Lhasa terrane, Tibet: Constraint from the zircon U–Pb geochronology of the gneisses. *Precambrian Research*, *237*, 64–77. https://doi.org/10.1016/j.precamres.2013.09.006

Liu, Q. S., Jiang, W., Jian, P., Ye, P. S., Wu, Z. H., & Hu, D. G. (2006). The zircon SHRIMP U-Pb age and petrochemical and geochemical features of Mesozoic muscovite monzogranite at Ningzhong, Tibet. *Acta Petrologica Sinica*, *22*, 643–652.

Ludwig, K. (2003). User's manual for Isoplot 3.00: A geochronological toolkit for Microsoft Excel. Kenneth R. Ludwig.

Ma, L., Wang, Q., Kerr, A. C., Yang, J.-H., Xia, X.-P., Ou, Q., et al. (2017). Paleocene (c. 62 Ma) Leucogranites in Southern Lhasa, Tibet: Products of Syn-collisional Crustal Anatexis during Slab Roll-back? *Journal of Petrology*, *58*(11), 2089–2114. https://doi.org/10.1093/petrology/egy001

Ma, L., Wang, Q., Wyman, D. A., Jiang, Z.-Q., Yang, J.-H., Li, Q.-L., et al. (2013). Late Cretaceous crustal growth in the Gangdese area, southern Tibet: Petrological and Sr–Nd–Hf–O isotopic evidence from Zhengga diorite–gabbro. *Chemical Geology*, *349*, 54–70.

Metcalfe, I. (2006). Palaeozoic and Mesozoic tectonic evolution and palaeogeography of East Asian crustal fragments: The Korean Peninsula in context. *Gondwana Research*, *9*(1-2), 24–46. https://doi.org/10.1016/j.gr.2005.04.002

Metcalfe, I. (2013). Gondwana dispersion and Asian accretion: Tectonic and palaeogeographic evolution of eastern Tethys. *Journal of Asian Earth Sciences*, *66*, 1–33. https://doi.org/10.1016/j.jseaes.2012.12.020

Middlemost, E. A. K., (1994). Naming materials in the magma/igneous rock system. *Earth-Science Reviews*, *37*, 215–224.

Mo, X., Hou, Z., Niu, Y., Dong, G., Qu, X., Zhao, Z., & Yang, Z. (2007). Mantle contributions to crustal thickening during continental collision: Evidence from Cenozoic igneous rocks in southern Tibet. *Lithos*, *96*(1-2), 225–242. https://doi.org/10.1016/j.lithos.2006.10.005

Mo, X., Zhao, Z., Zhou, S., & Huang, G. (2008). Complexity in ages and tectonic settings of Yarlung Zangbo Ophiolite Belt. 33rd International Geological Congress Workshop: Oslo, Workshop abstract.

Montel, J.-M. (1993). A model for monazite/melt equilibrium and application to the generation of granitic magmas. *Chemical Geology*, *110*(1-3), 127–146. https://doi.org/10.1016/0009-2541(93)90250-M

Niu, Y., Zhao, Z., Zhu, D.-C., & Mo, X. (2013). Continental collision zones are primary sites for net continental crust growth—A testable hypothesis. *Earth-Science Reviews*, *127*, 96–110. https://doi.org/10.1016/j.earscirev.2013.09.004

Patiño Douce, A. E., & Beard, J. S. (1996). Effects of P, f(O_2) and Mg/Fe ratio on dehydration melting of model metagreywackes. *Journal of Petrology*, *37*(5), 999–1024. https://doi.org/10.1093/petrology/37.5.999

Pearce, J. A. (1982). Trace elements characteristic of lavas from destructive plate boundaries. In R. S. Thorpe (Ed.), *Andesites* (pp. 525–548). New York: Wiley.

Pearce, J. A., Stern, R. J., Bloomer, S. H., & Fryer, P. (2005). Geochemical mapping of the Mariana arc-basin system: Implications for the nature and distribution of subduction components. *Geochemistry, Geophysics, Geosystems*, *6*, Q07006. https://doi.org/10.01029/02004GC000895

Peccerillo, A., & Taylor, S. R. (1976). Geochemistry of Eocene calc-alkaline volcanic rocks from the Kastamonu area, northern Turkey. *Contributions to Mineralogy and Petrology*, *58*(1), 63–81. https://doi.org/10.1007/BF00384745

Pichavant, M., Mysen, B., & Macdonald, R. (2002). Source and H_2O content of high-MgO magmas in island arc settings: An experimental study of a primitive calc-alkaline basalt from St. Vincent, Lesser Antilles arc. *Geochimica et Cosmochimica Acta*, *66*(12), 2193–2209. https://doi.org/10.1016/S0016-7037(01)00891-2

Pin, C., & Paquette, J.-L. (1997). A mantle-derived bimodal suite in the Hercynian Belt: Nd isotope and trace element evidence for a subduction-related rift origin of the Late Devonian Brévenne metavolcanics, Massif Central (France). *Contributions to Mineralogy and Petrology*, *129*(2-3), 222–238. https://doi.org/10.1007/s004100050334

Plank, T. (2005). Constraints from thorium/lanthanum on sediment recycling at subduction zones and the evolution of the continents. *Journal of Petrology*, *46*(5), 921–944. https://doi.org/10.1093/petrology/egi005

Plank, T., & Langmuir, C. H. (1998), The chemical composition of subducting sediment and its consequences for the crust and mantle, *Chemical Geology*, *145*(3–4), 325–394.

Rogers, N., Macdonald, R., Fitton, J. G., George, R., Smith, M., & Barreiro, B. (2000). Two mantle plumes beneath the East African rift system: Sr, Nd and Pb isotope evidence from Kenya Rift basalts. *Earth and Planetary Science Letters*, *176*(3-4), 387–400. https://doi.org/10.1016/S0012-821X(00)00012-1

Rudnick, R., & Gao, S. (2014). Composition of the continental crust. *Treatise on Geochemistry*, *4*, 1–51.

Rudnick, R. L., & Fountain, D. M. (1995). Nature and composition of the continental crust: A lower crustal perspective. *Reviews of Geophysics*, *33*(3), 267–309. https://doi.org/10.1029/95RG01302

Schellart, W., Lister, G., & Toy, V. (2006). A Late Cretaceous and Cenozoic reconstruction of the Southwest Pacific region: Tectonics controlled by subduction and slab rollback processes. *Earth-Science Reviews*, *76*(3-4), 191–233. https://doi.org/10.1016/j.earscirev.2006.01.002

Sengor, A. M. C. (1987). Tectonics of the Tethysides: Orogenic Collage Development in a Collisional Setting. *Annual Review of Earth and Planetary Sciences*, *15*(1), 213–244. https://doi.org/10.1146/annurev.ea.15.050187.001241

Shinjo, R., & Kato, Y. (2000). Geochemical constraints on the origin of bimodal magmatism at the Okinawa Trough, an incipient back-arc basin. *Lithos*, *54*(3-4), 117–137. https://doi.org/10.1016/S0024-4937(00)00034-7

Sláma, J., Košler, J., Condon, D. J., Crowley, J. L., Gerdes, A., Hanchar, J. M., et al. (2008). Plešovice zircon — A new natural reference material for U–Pb and Hf isotopic microanalysis. *Chemical Geology*, *249*(1-2), 1–35. https://doi.org/10.1016/j.chemgeo.2007.11.005

Spencer, C. J., Roberts, N. M. W., & Santosh, M. (2017). Growth, destruction, and preservation of Earth's continental crust. *Earth-Science Reviews*, *172*, 87–106. https://doi.org/10.1016/j.earscirev.2017.07.013

Stampfli, G. M., Hochard, C., Vérard, C., Wilhem, C., & vonRaumer, J. (2013). The formation of Pangea. *Tectonophysics*, *593*, 1–19. https://doi.org/10.1016/j.tecto.2013.02.037

Sun, S. S., & McDonough, W. (1989). Chemical and isotopic systematics of oceanic basalts: Implications for mantle composition and processes. *Geological Society, London, Special Publications*, *42*(1), 313–345. https://doi.org/10.1144/GSL.SP.1989.042.01.19

Taylor, S. R., & McLennan, S. M. (1985). *The continental crust: Its composition and evolution* (p. 312). Oxford: Blackwell Scientific Publications.

Torsvik, T. H., van der Voo, R., Preeden, U., Mac Niocaill, C., Steinberger, B., Doubrovine, P. V., et al. (2012). Phanerozoic polar wander, palaeogeography and dynamics. *Earth-Science Reviews*, *114*(3-4), 325–368. https://doi.org/10.1016/j.earscirev.2012.06.007

Valley, J., Lackey, J., Cavosie, A., Clechenko, C., Spicuzza, M., Basei, M., et al. (2005). 4.4 billion years of crustal maturation: Oxygen isotope ratios of magmatic zircon. *Contributions to Mineralogy and Petrology*, *150*(6), 561–580. https://doi.org/10.1007/s00410-005-0025-8

Wang, C., Ding, L., Zhang, L.-Y., Kapp, P., Pullen, A., & Yue, Y.-H. (2016). Petrogenesis of Middle–Late Triassic volcanic rocks from the Gangdese belt, southern Lhasa terrane: Implications for early subduction of Neo-Tethyan oceanic lithosphere. *Lithos*, *262*, 320–333. https://doi.org/10.1016/j.lithos.2016.07.021

Wang, D. B., Wang, L. Q., Yin, F. G., Sun, Z. M., Wang, B. D. & Zhang, W. P. (2012), Timing and nature of the Jinshajiang Paleo-Tethys: Constraints from zircon U-Pb age and Hf isotope of the Dongzhulin layered gabbro from Jinshajiang ophiolite belt, northwestern Yunnan, *Acta Petrologica Sinica*, *28*(5), 1542-1550.

Wei, G. J., Liang, X. R., Li, X. H., & Liu, Y. (2002). Precise measurement of Sr isotopic compositions of liquid and solid base using (LP) MCICP-MS. *Geochimica*, *31*, 295–305.

Wei, Y., Zhao, Z., Niu, Y., Zhu, D.-C., Liu, D., Wang, Q., et al. (2017). Geochronology and geochemistry of the Early Jurassic Yeba Formation volcanic rocks in southern Tibet: Initiation of back-arc rifting and crustal accretion in the southern Lhasa Terrane. *Lithos*, *278*, 477–490.

Wen, D. R., Chung, S. L., Song, B., Iizuka, Y., Yang, H. J., Ji, J., et al. (2008). Late Cretaceous Gangdese intrusions of adakitic geochemical characteristics, SE Tibet: Petrogenesis and tectonic implications. *Lithos*, *105*(1-2), 1–11. https://doi.org/10.1016/j.lithos.2008.02.005

Whitehouse, M., Claesson, S., Sunde, T., & Vestin, J. (1997). Ion microprobe U-Pb zircon geochronology and correlation of Archaean gneisses from the Lewisian Complex of Gruinard Bay, northwestern Scotland. *Geochimica et Cosmochimica Acta*, *61*(20), 4429–4438. https://doi.org/10.1016/S0016-7037(97)00251-2

Wilson, M. (1989). *Igneous Petrogenesis* (p. 466). Dordrecht: Springer. https://doi.org/10.1007/978-1-4020-6788-4

Winchester, J. A., & Floyd, P. A. (1977). Geochemical discrimination of different magma series and their differentiation products using immobile elements. *Chemical Geology*, *20*, 325–343. https://doi.org/10.1016/0009-2541(77)90057-2

Woodhead, J. D., Greenwood, P., Harmon, R. S., & Stoffers, P. (1993). Oxygen isotope evidence for recycled crust in the source of EM-type ocean island basalts. *Nature*, *362*(6423), 809–813. https://doi.org/10.1038/362809a0

Wu, F., Liu, C., Zhang, L., Zang, C., Wang, J., Ji, W., & Liu, X. (2014). Yarlung Zangbo ophiolite: Acritical updated view. *Acta Petrologica Sinica*, *30*, 293–325.

Wu, F.-Y., Jahn, B.-M., Wilde, S. A., Lo, C.-H., Yui, T.-F., Lin, Q., et al. (2003). Highly fractionated I-type granites in NE China (I): Geochronology and petrogenesis. *Lithos*, *66*, 241–273.

Xu, W.-C., Zhang, H.-F., Harris, N., Guo, L., Pan, F.-B., & Wang, S. (2013). Geochronology and geochemistry of Mesoproterozoic granitoids in the Lhasa terrane, south Tibet: Implications for the early evolution of Lhasa terrane. *Precambrian Research*, *236*, 46–58. https://doi.org/10.1016/j.precamres.2013.07.016

Yang, J., Xu, Z., Li, Z., Xu, X., Li, T., Ren, Y., et al. (2009). Discovery of an eclogite belt in the Lhasa block, Tibet: A new border for Paleo-Tethys? *Journal of Asian Earth Sciences*, *34*(1), 76–89. https://doi.org/10.1016/j.jseaes.2008.04.001

Yin, A., & Harrison, T. M. (2000). Geologic evolution of the Himalayan-Tibetan orogen. *Annual Review of Earth and Planetary Sciences*, *28*(1), 211–280. https://doi.org/10.1146/annurev.earth.28.1.211

Yuan, H.-L., Gao, S., Dai, M.-N., Zong, C.-L., Günther, D., Fontaine, G. H., et al. (2008). Simultaneous determinations of U–Pb age, Hf isotopes and trace element compositions of zircon by excimer laser-ablation quadrupole and multiple-collector ICP-MS. *Chemical Geology*, *247*(1-2), 100–118. https://doi.org/10.1016/j.chemgeo.2007.10.003

Zhang, L., Ren, Z.-Y., Nichols, A. R. L., Zhang, Y.-H., Zhang, Y., Qian, S.-P., & Liu, J.-Q. (2014). Lead isotope analysis of melt inclusions by LA-MC-ICP-MS. *Journal of Analytical Atomic Spectrometry*, *29*(8), 1393–1405. https://doi.org/10.1039/C4JA00088A

Zhang, L., Ren, Z. Y., Xia, X. P., Li, J., & Zhang, Z. F. (2015). IsotopeMaker: A Matlab program for isotopic data reduction. *International Journal of Mass Spectrometry*, *392*, 118–124. https://doi.org/10.1016/j.ijms.2015.09.019

Zhang, Z. M., Zhao, G. C., Santosh, M., Wang, J. L., Dong, X., & Liou, J. G. (2010). Two stages of granulite facies metamorphism in the eastern Himalayan syntaxis, south Tibet: Petrology, zircon geochronology and implications for the subduction of Neo Tethys and the Indian continent beneath Asia. *Journal of Metamorphic Geology*, *28*, 719–733.

Zhu, D. C., Mo, X. X., Zhao, Z. D., Niu, Y., Wang, L. Q., Chu, Q. H., et al. (2010). Presence of Permian extension-and arc-type magmatism in southern Tibet: Paleogeographic implications. *Geological Society of America Bulletin*, *122*(7-8), 979–993. https://doi.org/10.1130/B30062.1

Zhu, D. C., Pan, G. T., Chung, S. L., Liao, Z. L., Wang, L. Q., & Li, G. M. (2008). SHRIMP zircon age and geochemical constraints on the origin of Lower Jurassic volcanic rocks from the Yeba Formation, southern Gangdese, South Tibet. *International Geology Review*, *50*(5), 442–471. https://doi.org/10.2747/0020-6814.50.5.442

Zhu, D.-C., Zhao, Z.-D., Niu, Y., Dilek, Y., Hou, Z.-Q., & Mo, X.-X. (2013). The origin and pre-Cenozoic evolution of the Tibetan Plateau. *Gondwana Research*, *23*(4), 1429–1454. https://doi.org/10.1016/j.gr.2012.02.002

Zhu, D. C., Zhao, Z. D., Niu, Y., Mo, X. X., Chung, S. L., Hou, Z. Q., et al. (2011). The Lhasa Terrane: Record of a microcontinent and its histories of drift and growth. *Earth and Planetary Science Letters*, *301*(1-2), 241–255. https://doi.org/10.1016/j.epsl.2010.11.005